Title: An active electronic bidirectional interface for high resolution interrogation of the spinal cord

Authors: Samuel R. Parker, B.E.[1], Jonathan S. Calvert, Ph.D.[1], Radu Darie, Ph.D.[1], Jaeson Jang, Ph.D.[2,3], Lakshmi Narasimhan Govindarajan, Ph.D.[2,3,4], Keith Angelino, M.S.[5], Girish Chitnis, Ph.D.[5], Yohannes Iyassu, Ph.D.[5], Elias Shaaya, M.D.[6], Jared S. Fridley, M.D.[6], Thomas Serre, Ph.D.[2,3], Bryan L. McLaughlin, Ph.D.[5], David A. Borton, Ph.D.[1,3,6,7,*]

Affiliations:

1. School of Engineering, Brown University, Providence, RI, USA
2. Cognitive, Linguistic, and Psychological Sciences, Brown University, Providence, RI, USA
3. Carney Institute for Brain Science, Brown University, Providence, RI, USA
4. Integrative Computational Neuroscience (ICoN) Center, Massachusetts Institute of Technology, Cambridge, MA, USA
5. Micro-Leads Medical, Somerville, MA, USA
6. Department of Neurosurgery, Warren Alpert Medical School of Brown University and Rhode Island Hospital, Providence, RI, USA
7. Center for Neurorestoration and Neurotechnology, Providence VA Medical Center, Providence, RI, USA

* Corresponding author. Email: david_borton@brown.edu

Abstract

Epidural electrical stimulation (EES) has shown promise as both a clinical therapeutic tool and research aid in the study of nervous system function. However, available clinical paddles are limited to using a small number of contacts due to the burden of wires necessary to connect each contact to the therapeutic device. Here, we introduce for the first time the integration of a hermetic active electronic multiplexer onto the electrode paddle array itself, removing this interconnect limitation. We evaluated the chronic implantation of an active electronic 60-contact paddle (the HD64) on the lumbosacral spinal cord of two sheep. The HD64 was implanted for 13 months and 15 months, with no device-related malfunctions or adverse events. We identified increased selectivity in EES-evoked motor responses using dense stimulating bipoles. Further, we found that dense recording bipoles decreased the spatial correlation between channels during recordings. Finally, spatial electrode encoding enabled a neural network to accurately perform EES parameter inference for unseen stimulation electrodes, reducing training data requirements. A high-density EES paddle, containing active electronics safely integrated into neural interfaces, opens new avenues for the study of nervous system function and new therapies to treat neural injury and dysfunction.

Introduction

Epidural electrical stimulation (EES) of the spinal cord has been used for the treatment of neuropathic pain for almost six decades (Nahm, 2020), with over 50,000 procedures performed in the United States each year (Krog et al., 2023). In therapeutic or research applications, EES leads are surgically inserted into the epidural space on the dorsal aspect of the spinal cord and connected to an internal or external pulse generator (IPG or EPG, respectively) using inline contacts. Recently, EES has been used in preclinical research settings to study central,

peripheral, autonomic, and sensorimotor function (Calvert et al., 2023; Capogrosso et al., 2016; Gad et al., 2014; Musienko et al., 2012; Parker et al., 2013), as well as in clinical research settings to restore sensorimotor function following a spinal cord injury or amputation (Chandrasekaran et al., 2020; Lorach et al., 2023; Nanivadekar et al., 2023; Rowald et al., 2022). In parallel, epidural spinal recordings obtained through EES leads have been used as control signals for pain therapies (Nijhuis et al., 2023), to study voluntary movement control (Burke et al., 2021), and to examine somatosensory evoked spinal potentials (SEPs) (Nainzadeh et al., 1988; Woodington et al., 2024). However, all prior research studies and clinical applications utilize passive electronics, which constrains the number of contacts to a maximum of 32 channels, resulting in limited selectivity during stimulation and resolution during recording.

To ensure proper placement of the EES electrodes for activation of targeted spinal circuits, a key step is intraoperative testing during implantation (Falowski, 2019). During intraoperative testing, electrical stimuli are delivered through the implanted paddle. The stimuli primarily activate sensory neurons, which then recruit motor neurons via reflex pathways (Capogrosso et al., 2013). Using bilateral electromyography (EMG), the response of muscles at the same spinal level as the sensory targets is evaluated, and lead position is adjusted to achieve the desired placement (Shils and Arle, 2018). To recruit more specific pools of neurons on the spinal cord, multipolar stimulation is applied in a current steering approach (Chandrasekaran et al., 2020; Lorach et al., 2023; Mishra et al., 2023; Nanivadekar et al., 2023; Rowald et al., 2022), which requires access to multiple contacts in a confined region of interest. Subsequently, there have been efforts to design an EES paddle optimized for locomotor restoration, using neuroimaging data and computational modeling to guide the arrangements of contacts on the paddle (Rowald et al., 2022). The design of such EES paddles is constrained by the number of available stimulating contacts (16) while aiming to activate a long (59mm) span of the lumbosacral spinal cord. Utilizing current steering, significant improvement in motor function was observed despite large spacing between electrodes. However, the evoked motor response to EES is sensitive to lead placement, with movements as small as 1mm mediolaterally and 2mm rostrocaudally, resulting in a decrease in motor activation (Rowald et al., 2022). Lead migration is the most common complication following the implantation of an EES paddle (Logé et al., 2013) and can require costly revision surgeries (Harland et al., 2022). Misaligned stimulation may cause off-target effects, including activation of neighboring motor pools or uncomfortable paresthesias. Additional surgeries may be avoided if additional electrodes are available to stimulate in the new optimal location.

Stimulation parameter selection is a major barrier to the widespread adoption of EES for functional improvement after spinal cord injury (Solinsky et al., 2020). Consequently, there have been efforts to automate the optimization of stimulation parameters using machine learning models (Govindarajan et al., 2022; Zhao et al., 2021). Although these approaches have shown efficacy, prior models were conditioned on each electrode independently. Such an approach is effective for paddles containing low numbers of contacts but requires significant computing power to run many models in parallel for high-count paddles. Additionally, conditioning on each electrode independently does not allow the model to infer what may happen during stimulation

on electrodes excluded from the training set. As the number of stimulation contacts in a paddle increases, the time to collect training data scales linearly. Instead, if neural networks can infer the consequences of stimulation at unseen stimulation contacts, collecting training data from all contacts may not be necessary.

To address both placement limitations and stimulation parameter search optimization, a next-generation EES paddle must 1) enable localized current steering and bipolar re-referencing with densely packed electrodes, 2) span multiple spinal segments to target multiple sensorimotor pools, 3) be robust to typical lead migration observed in patients, and 4) be reconfigurable for patient anatomy. To meet these criteria, we designed and manufactured the HD64, a 60-contact epidural electrode paddle, with an onboard application-specific integrated circuit (ASIC) (Fig 1a, b). The onboard ASIC acts as a multiplexer, allowing 19 bidirectional channels to connect to any of the 60 contacts (Fig 1c-g). The reconfigurable nature enables the spatial layout of stimulating electrodes to be software-defined rather than fixed in hardware. The ASIC is powered and controlled by 5 of the 24 contacts on standard medical inline connectors, which have been used in implanted neuromodulation devices for decades (Letechipia et al., 1991) and are compatible with implanted pulse generators (IPG). A comparison between three commercial EES paddles with the work presented here can be found in Table 1. A visual comparison between the commercial paddles and the HD64 is presented in Fig. 1h.

To evaluate the HD64, two sheep were implanted with 1 and 2 electrode paddles for 13 and 15 months respectively (Fig 2a,b). During this time, our goals were to 1) identify device-related malfunctions, 2) quantify the selectivity of EES-evoked motor responses delivered using dense bipoles, 3) quantify differences in SEPs recorded using high- and low-density bipoles, and 4) extend the state-of-the-art stimulation parameter inference machine learning models to high-density electrodes (Govindarajan et al., 2022). A visual overview of the experimental setup is shown in Fig 2c.

Results

Successful chronic implantation of the HD64

To evaluate the safety of chronic implantation of the HD64 devices, we monitored the condition of the sheep continuously throughout the study and evaluated our ability to control the multiplexer on the active array. We successfully implanted two sheep with 1 (S1) or 2 (S2) HD64 EES paddles for 13 and 15 months, respectively. The multiplexers were configured 1598 and 4562 times on 34 and 51 unique days, respectively, throughout the study. No device-related malfunctions were observed, and control of the multiplexer remained stable. Over this time, we observed stable stimulation to EMG responses and spinal responses to spinal and peripheral stimulation. S2 was removed from the study after 15 months following a non-device-related adverse event.

High-density paddles enable precise motor recruitment

After implantation, we evaluated the benefit of a high-density electrode paddle in generating targeted motor recruitment from EES by recording motor-evoked responses from 6-8 bilateral lower extremity EMG sensors. Following EES, the EMG signal was rectified, then the area

under the curve (rAUC) was calculated and plotted as a function of amplitude (Fig. 3a). Applying monopolar EES to each of the 60 contacts in S1 produced a detectable motor response in at least 1 of 6 muscles. For each electrode contact, the EES amplitude required to reach 33% of the maximum activation for each muscle was identified (Fig. 3b). Contacts marked N.R. could not recruit the muscle to 33% of its maximum activation. Our analysis identified a lower EES amplitude required to recruit ipsilateral muscles than contralateral muscles, consistent with previous literature (Calvert et al., 2019). The results for S2 are presented in Fig. 3 – figure supplement 1.

The spatial diversity of EES-evoked motor responses was examined by performing unsupervised clustering. Uniform Manifold Approximation and Projection (UMAP) dimensionality reduction was performed on the recruitment data for each of the 60 electrodes. The low-dimensional embeddings were then clustered by statistical similarity. Eight independent clusters were identified. Electrodes for each cluster exhibited colocalization (Fig. 3c, Fig. 3 – figure supplement 2) on the HD64 paddle. To simulate the performance of a commercially available EES paddle (5-6-5, Medtronic, Minneapolis, MN), a scale drawing of the commercial paddle was overlaid on the HD64 clusters. While some commercial paddle contacts overlaid a single cluster, many contacts straddled two or more independent clusters, and Cluster 5 was not reachable (Fig. 3d). Consequently, the motor responses evoked using the commercial paddle may lack the fidelity available using the HD64. To explore the diversity of the recruitment patterns across clusters, the mean recruitment for each electrode in each cluster was calculated and then normalized using the Yeo-Johnson power transformation (Yeo and Johnson, 2000). Fig. 3e provides an example of the recruitment patterns observed for each cluster at a stimulation frequency of 50Hz.

To further explore the stimulation fidelity afforded using a high-density electrode paddle compared to a commercially available paddle, we examined the effect of current steering. EES was delivered using bipolar stimulation pairs spaced using the minimum inter-electrode spacing available on the HD64 (“narrow”, Fig. 4a and 4g), or the minimum spacing available on the 5-6-5 (“wide”, Fig. 4d and 4g), and was compared to each other, or a monopolar baseline (Fig. 4a and 4d). For each lower extremity muscle, the rAUC of the response to stimulation was calculated, as described previously. Using a Mann-Whitney U test, a significant difference was identified for all muscles at stimulation amplitudes greater than 1000μA in both bipolar configurations ($p < 0.05$), with some muscles displaying a significant difference from the monopolar configuration at the lowest amplitude tested (500μA) (Fig. 4b and 4e). Additionally, a significant difference was identified between the narrow and wide bipolar stimulations for all stimulation amplitudes ($p < 0.05$), though never in all muscles, indicative of a difference in the selectivity of activation (Fig. 4h). Additional current-steering configurations are shown in Fig. 4 – figure supplement 1.

We then sought to quantify the differences in the selectivity of EES-evoked motor recruitment. Selectivity indexes were plotted as a function of stimulation amplitude, and differences were assessed using a Mann-Whitney U test. The selectivity of stimulation evoked by the narrow bipolar field was significantly different from the monopolar stimulation at all EES amplitudes (Fig. 4c, $p < 0.05$). While the selectivity of the responses evoked by the wide field was

significantly different at lower amplitudes (≤ 1000μA), at larger amplitudes, there was no difference in selectivity between the wide bipolar field and monopolar stimulation ($p > 0.05$, Mann-Whitney U test) (Fig. 4f). Comparing the selectivity of the narrow and wide bipolar fields, a significant difference was identified in at least one muscle for all stimulation amplitudes. At the maximum EES amplitude tested (1500μA) 66% of instrumented muscles demonstrated unique stimulus selectivity (Fig. 4i).

High-density electrode paddles enable localized referencing

To evaluate the benefits of dense recording bipoles, we began examining epidural spinal responses to spinal and peripheral stimulation. The experimental configuration for this section is shown in Fig. 5a. To examine the propagation of evoked compound action potentials (ECAPs) on the spinal cord using the HD64, a EES bipole was created on the caudal midline of the paddle. Four bipolar recording pairs were established along the midline of the paddle, with centers distanced 7.3mm, 17.0mm, 26.7mm, and 31.6mm rostrally from the center of the stimulating bipole respectively (Fig. 5b). Single cathode-leading, biphasic, symmetrical EES pulses were delivered with amplitudes 2mA, 4mA, and 6mA. The pulse width remained constant at 25μs. The responses recorded by each bipole are presented in Fig. 5c. The elapsed time between stimulation and the peak of the ECAP was identified at each bipole for each of the 50 trials (Fig. 5d). Using the distance between the stimulating and recording bipoles and the time of peak response, the conduction velocity of the evoked response was calculated. For stimulation amplitudes 2mA, 4mA, and 6mA, the conduction velocities were 114.9m/s, 114.6m/s, and 111.8m/s, respectively.

We examined the SEPs in response to peripheral TENS application using three recording strategies, each containing six recording channels (Fig. 6a). The monopolar recording strategy used six consecutive HD64 contacts, with a recording reference wire implanted in the epidural space. The bipolar HD64 arrangement created six consecutive bipolar recording pairs using the minimum inter-electrode spacing available on the HD64. Finally, the bipolar 5-6-5 arrangement simulated the best-case bipolar arrangement using a commercial spinal paddle by creating six bipolar recording pairs with an interelectrode distance similar to that found on the Medtronic 5-6-5 (a to-scale drawing of this paddle is presented in blue in Fig. 6a). Fig. 6b shows the trial average (50 trials) SEP in response to 25V TENS applied to the right fetlock for all three arrangements. While the SEP is clearly prominent in the monopolar arrangement, the responses recorded by all channels are highly correlated. To identify the degree of correlation in recorded SEPs between channels, the mean pairwise zero-lag cross-correlation coefficient was calculated for each channel on single trials. The effect of arbitrary bipole orientation was removed by taking the absolute value of the correlation coefficient. A statistically significant difference between the distribution of correlations was identified for all recording arrangements ($p < 0.05$, Kruskal–Wallis test) (Fig. 6c). Spectral comparisons are made in Fig. 6 – figure supplement 1.

Continuous encoding of electrode position enables inference over electrode space

Increasing the number of stimulation contacts increases the solution space of automated parameter inference neural networks. We leveraged the dense grid of contacts on the HD64 to

enable spatial encoding of EES parameters during training and inference. The reparameterized neural network models were successfully trained to infer evoked EMG power following EES for all three electrode densities (Fig. 7a). The cumulative L1 loss between the predicted and actual EMG power for the held-out dataset is shown in Fig. 7b for each model. The L1 loss is inversely proportional to the number of electrodes in the training dataset. Significant differences were found between the full model and all other models, but not between the 50% and 25% models ($p < 0.05$, Kruskal–Wallis test). No significant difference in the L1 prediction error was identified between EES applied to electrodes in the training set or those excluded for the 25% and 50% models, indicating the network's ability to accurately infer the EMG response at unseen stimulation sites ($p > 0.05$, Mann-Whitney U test) (Fig. 7c). Decomposing the L1 loss by muscle reveals the same result identified previously, where the only significant difference in L1 distribution occurs between the 25% model and the remaining models ($p < 0.05$, Kruskal–Wallis test), except for the left gastrocnemius, where prediction loss followed the same distribution for all models ($p > 0.05$, Kruskal–Wallis test) (Fig. 7d).

Following successful amortization of spinal sensorimotor computations by the forward models, we performed inference using the inverse models to identify EES parameters predicted to evoke target EMG responses. The inverse models produced joint posterior density functions over stimulation parameters and electrode spaces for 32 target EMG vectors. Fig. 8a compares the posterior densities across the three models for a single EMG target. Posteriors for additional EMG targets are provided in Fig. 8 – figure supplement 1. Here, the 25% model predicts low likelihood across all electrode- and parameter-space. As the number of included electrode positions increases, the model localizes an optimal stimulation location, indicated by the focal region of high likelihood (Fig. 8b). To evaluate the performance of the models, we selected target EMG vectors from the held-out dataset for evaluation *in vivo*. The workflow and representative results are outlined in Fig. 8c. The stimulation parameter and electrode combination that produced the highest likelihood is identified and then delivered using the stimulator device. The evoked EMG responses from the six instrumented muscles are recorded and then compared offline to the target EMG vector. This process was repeated for all three models. We then compared the L1 error between the target EMG response and the evoked EMG response across models (Fig. 8d). A nonparametric Kruskal-Wallis test revealed that the underlying distributions of L1 errors between targets and the responses were not significantly different between models ($p > 0.05$). This indicates that adequate training data to infer stimulation parameters to faithfully reproduce target EMG activity could be collected using a sparse subset (25%) of the available stimulation contacts. Further, no significant differences were observed between the re-sent stimulation parameter (the "ground truth") distribution and the proposal distributions. This indicates that the parameter inference performance approached the soft upper bound given by the natural variations in EMG recorded across time.

Discussion

In this work, we presented a novel, high-density, active electronic epidural electrical stimulation paddle, the HD64. We quantified the improvements in the selectivity of motor responses evoked using the HD64 compared to the wider bipolar configurations available using the Medtronic 5-6-5 spacing as a guide. Further, we demonstrated the capabilities of the HD64 to provide superior

referencing of somatosensory evoked potentials following peripheral nerve stimulation, significantly reducing the mean spatial correlation compared to bipoles with similar spacing to commercial paddles. Finally, we extended the current state-of-the-art stimulation parameter inference model to encode sensorimotor-EES relations, enabling increased spatial resolution of inferred EES parameters and utilizing 2.5x higher channel count compared to prior work. In summary, the active multiplexing of the HD64 provides an increased channel count, enabling increasing stimulation, recording, and parameter inference specificity.

Onboard active multiplexing provides functional benefits

Our novel paddle contains an active multiplexing chip hermetically sealed on the body of the EES paddle, enabling contact with 60 bidirectional contacts through two 12-contact percutaneous lead tails. The increased contact density combinatoriality increases the number of possible stimulation configurations available for research and therapeutic applications. In contrast to this reconfigurability, current clinically available EES paddles sacrifice spatial resolution in favor of a general, “one-size-fits-most” approach. In research studies, prior work has suggested a library of paddles of different sizes to suit person-to-person variability in anatomy (Rowald et al., 2022). Instead, the reconfigurability of the HD64 allows for localized concentration of stimulating electrodes to activate a specific area of the spinal cord, enabling focal stimulation with current steering to prevent off-target effects without sacrificing the ability to simultaneously stimulate other distal regions.

As the first example of an EES paddle including active electronics, we were particularly interested in assessing the ability of the encapsulant to maintain patency during chronic implantation. We found that the HD64 remained functional for at least 13 months after implantation and did not display symptoms of fluid ingress. Communication between the externalized stimulation and recording hardware and the onboard multiplexer remained robust throughout the study. This initial result is promising for the future of epidural medical devices containing active electronics. With current technologies, chips of similar dimensions to that developed here are capable of significant computational power. Our result may open the door for diverse advances in on-paddle processing, including signal processing or closed-loop stimulation parameter control. While additional testing and regulatory approval is required before such technologies can be translated into clinical applications, this demonstration represents a promising first step.

Our study benefits from decades of prior research showing the selective activation of motor neuron pools using EES applied to the lumbosacral spinal cord. Specifically, EES has been utilized heavily to restore walking ability following a spinal cord injury (Angeli et al., 2018; Capogrosso et al., 2016; Gill et al., 2018). Other studies have used EES to establish somatotopic maps of stimulation location to recruited lower limb extremities (Calvert et al., 2019; Hofstoetter et al., 2021). Extending the number of possible stimulation contacts to 60 places multiple stimulating contacts in close proximity, which may lead to redundancy in the populations of neurons they recruit. To quantify this redundancy, we performed spectral clustering on the monopolar EMG recruitment data. By a silhouette analysis, we found that the responses of stimulation on the full set of electrodes could be explained by eight stereotyped

clusters of statistically similar motor recruitment. All but one cluster contained multiple electrode contacts. This redundancy may prove the HD64 is more robust to lead migration. In the case of such migration, the target region will likely still be accessible by neighboring stimulation contacts on the HD64. Additionally, should a stimulation contact become damaged or nonfunctional, the HD64 can be reconfigured using the onboard ASIC to instead provide stimulation to an intact contact in the same cluster, avoiding costly and invasive revision surgeries.

Finally, our work quantified the improvements in lower extremity EMG recruitment offered by bipolar stimulation and examined the impact of bipolar pair spacing. Compared to monopolar stimulation, significant differences in selectivity were identified in both narrow and wide bipolar configurations. This result has also been identified by other groups investigating cochlear and sciatic nerve stimulation (Maciejasz et al., 2013; Zhu et al., 2012). While the differences in selectivity were more apparent between the narrow bipolar and monopolar configurations at higher amplitudes, these differences were less apparent at high amplitudes compared to low amplitudes for the wide bipolar configuration. This suggests a narrow bipolar configuration may be the optimal choice for restorative motor EES, maintaining selectivity while providing robust recruitment for functional limb utilization.

Spinal local field potential spatial correlation is proportional to bipole contact separation

Recording EES-evoked spinal responses, or ECAPs, can provide quantitative data regarding EES paddle status. ECAPs have been used as a control signal for pain-modulating EES (Mekhail et al., 2020), and we have previously suggested their utility in the identification of neural anatomy (Calvert et al., 2023). Using bipolar recording configurations on the HD64, we observed an orthodromically propagating response to EES. The conduction velocities of these responses are consistent with the published ranges for Type Ia and Ib axons, which have been shown to be recruited by EES in computational models (Capogrosso et al., 2013).

Our work demonstrates the formation of dense recording bipoles on the ovine spinal cord, and uses these recording bipoles to examine EES- and TENS-evoked spinal responses. This is timely for the field of neural interfaces, with the recent advent of high-density neural probes (Chamanzar et al., 2023; Jun et al., 2017; Steinmetz et al., 2021) and electrocorticography (ECoG) grids (Palopoli-Trojani et al., 2024; Rachinskiy et al., 2022). As in prior work, we set out to investigate the utility gained with increases in recording density. By placing electrodes closer together, the number of neurons recorded by each bipole decreases, and local variations in neural activity are highlighted rather than being conglomerated into a population response. Consequently, the SEPs recorded by monopolar electrode configurations are highly spatially correlated across the span of the electrode. Here, we show that this spatial correlation is greatly reduced by introducing bipolar recording and can be reduced further by decreasing the spatial separation of the recording cathode and anode. Using conventional EES paddles, contacts are sparsely distributed to ensure coverage of a large area using a small number of electrodes. This sets a minimum limit on contact separation. We suggest that using the HD64, dense recording bipoles can be created at arbitrary points of interest. Further, contact separation can be non-uniform (for example, tight spacing in regions of high spatial variability and wider spacing in less

volatile regions) or change with time or desired function (creating activity-dependent paddle arrangements).

EES can be spatially encoded for parameter inference over arbitrary channels

Stimulation parameter inference remains an obstacle to widespread clinical implementation of EES (Solinsky et al., 2020). Our previous parameter selection automation work (Govindarajan et al., 2022), and other subsequent literature (Bonizzato et al., 2023) treat stimulating electrodes as discrete variables. As such, spatial relationships (such as those uncovered in Fig. 3d) cannot be leveraged by the model. In this work, we instead evaluated a novel electrode encoding scheme that accounts for spatial relationships between electrode contacts. This approach is extensible to very high channel counts and allows the network to identify optimal stimulation locations not included in the training dataset.

As the number of available stimulation channels increases, the time required to collect training data from every contact scales linearly. Unaddressed, this is a barrier to clinical translation of parameter selection automation techniques and high-density EES paddles. Here, our work shows that exhaustive sampling of every stimulation contact is not required if the electrode encoding scheme is continuous. No significant decrease in EMG response prediction performance is observed for electrode inclusion rates as low as 50%, and stimulation parameter inference performance did not significantly vary across inclusion rates tested. The development of efficient machine learning tools, such as the one presented in this manuscript, greatly reduces the amount of training data required. Increasing efficiency and decreasing data collection efforts will aid in scaling EES for clinical use, which could yield meaningful benefits during spinal rehabilitation in patients with neural dysfunction.

Study limitations and implications for future research

Our study introduces a high-density EES paddle with an integrated multiplexer and demonstrates the utility of increased electrode density. However, several limitations should be considered. While the characterization presented in this manuscript empirically supports the use of high-density electrode paddles in these applications, a more thorough assessment may be possible using computational models. Previous advances in electrode design were informed by finite element models of 15 healthy volunteers (Rowald et al., 2022). Such models could quantify recruitment of off-target motor neuron pools after applying stimulation at bipoles of various sizes, however the work presented here utilizes an ovine model. The spinal cord of the sheep is similar to that of humans in terms of gross anatomy and size and has been used as a model for the study of spinal electrophysiology (Calvert et al., 2023; Chakravarthy et al., 2020; Parker et al., 2020, 2013), but results of this manuscript may not be generalizable to human anatomy. A computational model of the ovine spinal cord may further validate our findings. Future studies are required to evaluate the therapeutic potential of high-density EES electrodes or to quantify the effect of stimulation focality on behavioral values such as sensation. One current barrier to clinical translation of the HD64 is the lack of existing implantable pulse generators (IPGs) capable of generating the power and communication signals necessary to control the onboard multiplexer. Additionally, the inclusion of active electronics in implanted electrodes increases the power draw of the implantable system, and must be considered when

selecting an appropriate IPG battery size, though the HD64 consumes only 20μA tonically and 100μA when reconfiguring. Our neural network models demonstrate sufficient accuracy to match EMG patterns, however, these experiments were conducted with the sheep at rest and elevated in a sling. A more functional task may instead consider applying a stimulation sequence to match a target kinematic trajectory. Additionally, our neural network parameter inference is limited to monopolar stimulation patterns and, therefore, cannot take advantage of the improved selectivity identified by bipolar stimulation in this manuscript. Bipolar stimulation dramatically increases the number of electrode configurations the network must evaluate; the additional complexity of which is a promising target for future research.

Methods

Design of the 60-channel active paddle (HD64)

To extend the therapeutic span of EES delivery, there is a need to spatially extend treatment beyond the dorsal columns to the dorsal horn and dorsal roots. Extending the treatment surface area using a fixed number of electrodes would result in a sparser electrode density and a reduced targeting resolution of spinal fibers. With conventional implanted lead and connector technology, each additional electrode requires one additional lead conductor and connector contact, thus limiting the scalability of the therapy treatment area. Current pulse generator implementations are limited by ball-spring connector technology. Wiring 32 electrodes currently requires four lead-tails which does not easily scale to 64 electrodes.

The HD64 is a high-resolution active-multiplexed lead technology developed to break this constraint by performing multiplexing within the distal electrode to enable 20+ input wires to be dynamically and programmably connected to 60+ surface electrodes. To realize an active-multiplexed electrode array, we developed multiple technology components including: 1) a high-voltage, AC-powered 24:64 multiplexing ASIC, 2) high-density hermetic feedthrough technology, 3) precision electrode technology (100μm platinum-iridium lines and 100μm spaces), and 4) medical-grade micro-bonding integration processes. Integration of the active paddle combined high-precision techniques with established medical-grade processes and materials. We utilized validated hermetic sealing methods and known materials while completely avoiding semiconductor processes and processing aids, which use unproven chemistries for long-term reliability.

<u>High-voltage 24:64 multiplexing ASIC with AC power and charge-balanced programming</u>

We developed a 24-input, 64-output multiplexing ASIC to enable multiplexed stimulation and recording. Fabrication was performed using the X-FAB XH035A 18V 350 nm silicon process to construct the ASIC with a ball-grid array to facilitate flip-chip solder bonding (Fig 1d). The multiplexer can be dynamically programmed with a two-wire interface to connect any of 20 inputs to any of 64 outputs. The multiplexer contains 64 blocks, each containing four switches to ensure every output electrode has a redundant connection to at least four stimulation/recording inputs. The ASIC operates from AC power (5V AC, 10-500 kHz) to allow for charge-balanced power to the ASIC to be provided by an IPG. Charge balance is necessary to prevent corrosion and long-term electro-migration of the conductors. The ASIC uses an on-board rectifier with off-chip capacitors to convert the AC signal to +/-9V DC internally and 3.3V.

440
441 High-density hermetic electronics package
442 We developed a 93-feedthrough ceramic assembly (8 x 8 x 0.75 mm) brazed into a titanium
443 flange. On the interior of the package, the ASIC was flip-chipped (not shown) to the surface of
444 the feedthrough array (Fig 1e). A low-outgassing underfill was applied between the ASIC and
445 the ceramic and inspected for voids. Surface mount capacitors were solder-attached to gold
446 features on the ceramic feedthrough surface. On the exterior of the hermetic packaging, the
447 feedthroughs emerged from the ceramic surface (Fig 1f). A moisture getter was applied to the
448 interior titanium lid, which was then seam-welded to form a hermetic assembly. The assemblies
449 were measured for hermeticity to a leakage of $2x10^{-10}$ atm-cc/s using a laser interferometer
450 method, which complies with hermeticity standard MIL-STD-883 Method 1014.15.
451
452 Precision electrode technology
453 Precision electrode technology was used to make a delamination-free electrode using medical-
454 implant grade silicone (Nusil, Carpentaria, CA), platinum-iridium 90/10 conductors, and a mesh
455 reinforcement layer (Fig 1g). In this process, the silicone and platinum-iridium were pre-
456 processed using a proprietary laser patterning technique, resulting in 50-100 μm electrode
457 features in 12-50 μm thick platinum-iridium 90/10. A flexible reinforcement mesh layer was
458 embedded within the silicone to prevent stretching of the silicone to protect the electrode traces
459 from fracture during stretching or repetitive pull cycles. The HD64 paddle consists of three
460 silicone and two metal layers for a total substrate thickness of 400 μm. Using a proprietary
461 process, the silicone layers were chemically fused together in a seamless and delamination-free
462 construction.
463
464 Electrode-hermetic electronics integration
465 The completed hermetic electronics assembly and high-density electrode assembly were then
466 micro-bonded using a precision process. Mechanical alignment fixtures were used to align
467 receiving pads on the electrode array with the feedthrough pins. Machine vision was used to
468 inspect the tolerances of the electrode, and the feedthrough component and components with
469 >35 μm of tolerance were discarded to ensure reliability of the bonding process. After the
470 precision mechanical alignment was performed, a custom-made machine was developed to
471 perform sequential thermal welding between each platinum-iridium pad and each platinum-
472 iridium feedthrough.
473
474 Injection molding and lead-tail attachment
475 Lead-tails with 12 conductors and a 12-contact ring connector were manufactured and welded
476 to the platinum-iridium receiving pads on the HD64 substrate. A silicone injection molding step
477 was used to create the contoured paddle back-side shape of the HD64, as well as to completely
478 insulate between all of the feedthrough pins. A fixture and process were developed to ensure
479 the silicone flow did not trap bubbles during the assembly process.
480
481 Control of Active-Multiplexing
482 Establishing digital control and maintaining knowledge of the state of the HD64 multiplexer was
483 necessary to demultiplex the recorded spinal responses and stimulation information *post-hoc.* A

484 schematic representation of the connections and devices used in this manuscript is presented in
485 Fig. 2c. The HD64 is powered and controlled by an external device (MB-Controller, Micro-Leads
486 Medical, Somerville, MA), which communicates with a host PC over a serial connection.
487 MATLAB (version 2023b, MathWorks, Natick, MA) functions were provided to connect to,
488 configure, and read from the multiplexer. Stimulation was also controlled using Matlab. A
489 custom script was written to ensure that the multiplexed stimulation channel was connected to
490 the target electrode contact. Additionally, changes to the multiplexer configuration were logged
491 alongside stimulation information, allowing synchronization with the recorded electrophysiology.
492 This enabled recorded multiplexed signals to be split as the multiplexer configuration changed
493 and a sparse 60 x *n* matrix of demultiplexed signals to be created, where *n* is the recording
494 length in samples.
495
496 Connecting the HD64 to the analog headstages required custom hardware. The HD64 lead-tails
497 contain both spinal signals, stimulation pulses, digital control, and AC power signals. A custom
498 PCB was created to route these signals to their respective targets (i.e., spinal signals to the
499 input pins of the Macro+Stim (Ripple Neuro, Salt Lake City, UT), and the digital power and
500 control signals to the MB-Controller). A second PCB was created to route signals to an A-M
501 Systems Model 1800 (Carlsborg, WA) recording unit. As this recording unit only supported two
502 channels, the additional HD64 channels were not routed through the multiplexer. Finally, a
503 custom, fully-implanted stimulation and recording device was constructed with an onboard field-
504 programmable gate array (FPGA) capable of controlling the HD64, eliminating the need for an
505 additional PCB.
506
507 ***In vivo* evaluation**
508 All surgical and animal handling procedures were completed with approval from the Brown
509 University Institutional Animal Care and Use Committee (IACUC), the Providence VA Medical
510 System IACUC, and in accordance with the National Institutes of Health Guidelines for Animal
511 Research (Guide for the Care and Use of Laboratory Animals). All methods described in this
512 study follow the Animal Research of *In V*ivo Experiments (ARRIVE) guidelines. Two sheep (both
513 female, aged 4.19±0.3 years, weighing 92.5±2.5kg) were used for this study. Recordings were
514 performed with Sheep S1 and S2 for 13 months and 15 months, respectively. Animals were
515 kept in separate cages in a controlled environment on a 12-hour light/dark cycle with *ad libitum*
516 access to water and were fed twice daily. The ovine model was chosen for this study as the
517 spine and spinal cord are comparable in size and share many anatomical features with humans,
518 and the use of the ovine model to study the spinal cord has been well established (Marcus et
519 al., 1997; Parker et al., 2020, 2018, 2013; Reddy et al., 2018; Wilson et al., 2017).
520
521 <u>Surgical procedures</u>
522 The sheep were implanted, as previously reported (Calvert et al., 2023). However, S1 was
523 implanted with a single paddle due to a narrow epidural space at L3. Briefly, under propofol-
524 based general total intravenous anesthesia (TIVA), an L4 – L6 laminectomy with medial
525 facetectomy was performed. The rostral HD64 paddle (if included) was gently placed, then slid
526 rostrally, after which the caudal paddle was placed. Strain relief loops were made, and then the
527 lead-tails were tunneled to the skin, where they were externalized. Reference and ground

electrodes (Cooner AS636 wire, Cooner Wire Company, Chatsworth, CA) were secured epidurally and in the paraspinal muscles, respectively. Strain relief loops were made, and these wires were also tunneled then externalized. Intraoperative testing was used to confirm device functionality. The animals were allowed to recover from anesthesia then returned to their pens.

A second surgical procedure was performed to place intramuscular EMG recording equipment (L03, Data Sciences International, St. Paul, MN) in the lower extremity musculature of S1. The sheep was intubated and placed prone on the operating table. The sheep was placed in a V-shaped foam block to maintain stability throughout the procedure, and a rectangular foam block was placed under the hip to alleviate pressure on the hindlegs (Calvert et al., 2023). The legs were dangled laterally off of the operating table, and each of the hooves was placed in a sterile surgical glove and wrapped in a sterile bandage for manipulation during the procedure. On each side, the *extensor digitorum longus*, *biceps femoris*, and *gastrocnemius* were identified by palpating anatomic landmarks. Small incisions were made over the bellies of each of the three muscles to be instrumented, and a small subcutaneous pocket was made on the flank. All three channels were tunneled from the subcutaneous pocket to the most proximal muscle. There, a single recording channel and its reference wire were trimmed to length and stripped of insulation. The bare electrodes were inserted into the muscle belly perpendicular to the muscle striations, through 1-2cm of muscle. The electrodes were secured by suturing to the muscle at the insertion and exit points of the muscle belly. The remaining two channels were tunneled to the next muscle, where the process was repeated before the final electrode was tunneled to the most distal muscle and secured in the same manner. Finally, the telemetry unit was placed in the subcutaneous pocket on the upper rear flank and secured using a suture. Approximately 0.5g of Vancomycin powder was irrigated into the subcutaneous pocket, and the pocket was closed. The process was then repeated on the other side. After brief intraoperative testing, the animal was allowed to recover from anesthesia then returned to its pen.

<u>Recording of EES-evoked motor potentials</u>

At the beginning of the experimental session, the awake sheep was hoisted in a sling (Panepinto, Fort Collins, CO) until clearance between its hooves and the floor was observed. The HD64 was connected, enabling simultaneous stimulation, recording, and control of the multiplexer. Stimulation amplitude ranges were identified for each sheep, ranging from below motor threshold to the maximum comfortable response above motor threshold. Five stimulation amplitudes were selected in the comfortable range, and each stimulation was delivered at four frequencies (10, 25, 50, and 100Hz).

In monopolar stimulation trials, stimulation was independently applied to each of the 60 contacts. A cathode-leading, 3:1 asymmetrical, charge-balanced waveform was used in all cases. The cathodic-phase pulse width was 167μs, and the stimulation train duration was 300ms. The stimulation anode was the implanted reference wire in the paraspinal muscles. The inter-train interval was randomly drawn from a uniform distribution spanning 1-2 seconds, and stimulus presentation order was randomized.

In bipolar stimulation trials, bipolar pairs were defined such that the spacing between the cathode and anode represented the minimum spacing possible on either the HD64 or Medtronic 5-6-5 paddles. Here, stimulation was provided at 5 amplitude values in the comfortable range for each sheep at a frequency of 10Hz. This 100ms inter-pulse-interval was selected to maximize the latency between stimuli so that the neural response to the previous pulse had completely subsided prior to the delivery of the subsequent stimulation. The stimulation waveform shape, train duration, and inter-train interval were unchanged from the monopolar trials. Stimulation presentation was again randomized.

Data was collected during stimulation across 60 electrode contacts per spinal paddle and 6-8 EMG channels. The spinal, EMG, and stimulation data were synchronized by injecting a known bitstream into the time series data of the spinal and muscular recordings. Stimulation sessions did not exceed three hours, and the sheep were constantly monitored for signs of distress and fed throughout each session. At the conclusion of recording, the animal was returned to their pen.

Recording of EES-evoked spinal potentials

At the beginning of each session, the awake sheep was hoisted in a sling, and the HD64 was connected as described previously. The HD64 was routed to create a stimulating bipole between the caudal-most midline electrodes and a recording bipole, either 7.3mm, 17.0mm, 26.7mm, or 31.6mm more rostral than the stimulating bipole. As the recording device (A-M Systems Model 1800) consisted of only two recording channels, each of the bipoles was recorded sequentially. For each stimulation event, a cathode-leading, symmetrical EES pulse was delivered to the stimulation bipole. The EES amplitude was set to 2mA, 4mA, and 6mA, while the width of the cathodic phase was kept constant at 25μs.

Recording of TENS-evoked spinal potentials

With the sheep hoisted in the sling apparatus, the bony anatomy of the right-side hind fetlock was palpated, and a ring of wool just proximal to the fetlock was shorn, extending approximately 10cm proximally. The exposed skin was cleaned with isopropyl alcohol, which was allowed to air dry. 2”x 2” TENS (Transcutaneous Electrical Nerve Stimulation) patches (Balego, Minneapolis, MN) were cut to size, placed on the medial and lateral aspects of the cannon bone, then connected to the stimulator device (Model 4100, A-M Systems Inc, Carlsborg, WA). The stimulation monitoring channel was connected to an analog input on the EMG system for synchronization. Stimulation amplitude was set to 25V, and stimulation pulse width was 250μs. The interstimulus interval was 500ms. The above process was then repeated for the left hindlimb.

Extension of state-of-the-art EES parameter inference neural networks

Model reparameterization and data acquisition

To extend the state-of-the-art EES parameter inference neural network models to 60 electrodes, the input space was reparameterized. The original model accepted a 3D input feature vector: amplitude, frequency, and electrode index (Govindarajan et al., 2022). The new model used here now accepts a 4D input vector: amplitude, frequency, electrode mediolateral coordinate,

and electrode rostrocaudal coordinate (i.e., inputting an x-y location rather than hardcoding an arbitrary electrode number). By defining the electrode position on a continual space, positional relationships between each electrode could be learned. As in the original model, frequency and amplitude values were normalized to the range [0, 1).

For each sheep, radiographs were collected following the implantation of the HD64 electrodes. By examining the orientation of each electrode contact, an affine transformation was computed to account for skew between the electrode paddles and the radiograph camera. In this transformed space, the relative position of the rostral paddle (if placed) was determined with respect to the caudal paddle. Using the known dimensions of the HD64, the coordinates of each electrode contact were calculated. The electrode coordinates were normalized to the same range as the amplitude and frequency (the left-most caudal electrode contact had a coordinate of (0, 0), with increasing values extending rightward and rostrally).

The data acquisition phase proceeded as described for recording of monopolar EES-evoked motor responses.

Data handling & evaluation

The data handling and preprocessing steps were performed as previously described (Govindarajan et al., 2022). Briefly, the EMG recordings from bilateral *extensor digitorum longus*, *biceps femoris*, and *gastrocnemius* were high-pass filtered at 3Hz, then a second-order infinite impulse response notch filter with a quality factor of 35 at 60Hz. EMG envelopes were calculated by computing the moving RMS (root mean squared) value of each signal for a 300ms window (50% window overlap). The enveloped data was epoched from 100ms prior to the onset of stimulation to 300ms after the conclusion of the stimulation train (700ms epochs). The epoched data was labeled with the stimulation amplitude, frequency, and electrode coordinates determined by the map described previously. This dataset was the 100% density dataset, as it contained every stimulation electrode. The 50% density dataset was created by removing 30 electrode contacts from the 100% density dataset. Finally, the 25% density dataset was created by removing an additional 14 contacts from the 50% density dataset. The remaining data handling steps (outlier removal, unreliable sample removal, subthreshold EMG removal, and EMG summarization) were performed as previously described (Govindarajan et al., 2022). Independent models were then trained for each density dataset.

Following the completion of training and inference, stimulation proposals were generated for a set of target EMG responses obtained from testing EES parameter sets (40% of all conditions were held out, as in (Govindarajan et al., 2022)). Since these testing data were held out from the training data (the remaining 60% EES parameter conditions), the combination of target EMG responses and their EES parameters has never been shown to the network during the training phase. Proposals to achieve these target EMG responses were generated independently by all three models. If the stimulation contact coordinate inferred for a proposal was not encircled by a stimulation contact, the proposal was snapped to the nearest contact. The proposed stimulation amplitudes were checked to comply with the ranges the researcher found comfortable for each sheep and through software limits. To assess changes in the distribution of evoked motor

responses, a set of stimulation parameters applied during the collection phase were repeated at the start of the evaluation phase. Then, each proposal was delivered 10 times, and the proposal order was randomized. After collection, the L1 error between the proposed EMG response and the achieved EMG response was calculated.

Statistics and Data Processing

Following the completion of an experimental session, the recorded data were analyzed offline using custom-written code in MATLAB (R2023b) and Python 3.8.17 (using SciKit-Learn version 1.4.1 (Pedregosa et al., 2011) and Uniform Manifold Approximation and Projection (UMAP) module (McInnes et al., 2018b)). To compute recruitment curves, the recorded EMG signals were split into 500ms stimulation-triggered epochs. This epoch length was selected to capture the 300ms pulse train and residual motor effects. The data was then rectified, and the power was recruited by taking the absolute value and then summing all samples in each epoch. The power values were then normalized to a range of [0, 1] for each muscle by subtracting the minimum activation and dividing by the range of activations. The EMG power (rectified area under the curve, or rAUC) was averaged across the four stimulation trials for each amplitude, frequency, and electrode combination, and the standard deviation was computed. To identify statistical clusters of evoked EMG responses, the single-trial recruitment data was rearranged into a 2D table, where rows were stimulation electrodes, and the recruitment data for each stimulation frequency was horizontally concatenated to form the columns. Raw rAUCs were normalized using the Yeo-Johnson power transformation (Yeo and Johnson, 2000), and used as input features for the Uniform Manifold Approximation and Projection (UMAP) algorithm (Gorman, n.d.; McInnes et al., 2018a). A two-dimensional embedding was generated, where each point represents the rAUC response pattern across muscles, stimulation amplitudes, and frequencies for a given electrode (four points per electrode, corresponding to the four stimulation repetitions). Spectral clustering (Shi and Malik, 2000) was used to identify between 1 and 16 clusters of electrodes in the dataset, representing groups of electrodes with similar rAUC response patterns. A silhouette analysis (Rousseeuw, 1987) indicated that the optimal number of clusters was eight. If the four repeats of the same electrode did not fall into the same cluster, that electrode was assigned the cluster label corresponding to the majority of the four labels. The process of epoching, rectifying. and integrating the EMG signal was repeated for the bipolar stimulation datasets. Before normalizing the bipolar data, the unnormalized monopolar data was included such that both monopolar and bipolar EMG responses were normalized to the same range. The EMG distributions for each stimulation configuration were compared using a Mann-Whitney U test. This non-parametric test was selected as it does not assume normality of the underlying distributions. Finally, the selectivity indexes were computed for each muscle in all stimulation electrode configurations (Badi et al., 2021; Bryson et al., 2023). The distributions of selectivity indexes were also compared using a Mann-Whitney U test.

Spinal evoked compound action potentials (ECAPs) and SEPs were first split into 500μs and 100ms stimulation-triggered epochs, respectively. The epochs were averaged across 50 stimulation trials and filtered with a low-pass filter at 2000Hz. The mean and standard deviation of the ECAPs were calculated for each amplitude and recording bipole. The latency of the peak of the response was identified for each of the 50 single trials. A linear fit of the latency-distance

relationship was calculated, and the gradient of this fit was calculated to determine the conduction velocity. The SEPs were re-referenced by subtracting the inverting electrode recording from the non-inverting electrode recording for each recording bipole. The mean SEP response was calculated for each recording channel. To assess the spatial correlation between recorded channels, the normalized zero-lag cross-correlation coefficient was computed between each recording channel for single trials. For each channel, the mean pairwise correlation to other channels was calculated over each trial. To assess the uniqueness between channels, the absolute value of the correlation was computed and then subtracted from 1. That is, perfectly correlated channels, with a mean pairwise correlation coefficient of 1, would receive a score of 0, while completely uncorrelated channels would receive a score of 1. The distribution of uniqueness scores was compared using a Kruskal-Wallis test. This non-parametric test was selected as it does not assume normality of the underlying distributions.

To evaluate the performance of the EMG response simulation neural network (the forward model), the L1 loss was computed by subtracting the predicted EMG vector from the evoked EMG vector and then taking the absolute value. This process occurred on a held-out dataset of mean EMG responses to 480 stimulation combinations, each with 4 repeats. The distributions were compared using a Kruskal-Wallis test. The random performance of each network was determined by generating a randomized prediction for each muscle from a uniform distribution ranging from 0 to the maximum response in the training dataset. Then, this randomized EMG vector was compared to the target vector. The L1 losses were split for each model by inclusion of the stimulating electrode in the training dataset. The L1 losses were compared within models using the Mann-Whittney U test. Finally, the L1 losses were split for each model by muscle, and their distributions were compared using a Kruskal-Wallis test. To evaluate the performance of the parameter inference neural network (the inverse model), the rAUC was computed for each of the responses to inferred parameters. The mean L1 error between the predicted and achieved EMG rAUC vectors was calculated across muscles. Additionally, the L1 error between the EMG responses to the original EES parameters and the responses to these same parameters sent during the evaluation session (which occurred some hours after the training session) was calculated. The distributions of L1 errors were compared using the Kruskal-Wallis test.

Acknowledgments

We would like to thank Aaron Gregoire and the Center for Animal Resources and Education (CARE) staff at Brown University for their assistance with animal care, as well as Alison Gorbatov and Krista Tocco from the Center for Neurorestoration and Neurotechnology (CfNN) for their assistance with the Providence VA Medical System regulatory work. We would also like to thank John Murphy for his engineering expertise in designing modifications to the sling apparatus. Finally, we would like to thank Moses Goddard for his surgical time and expertise in implanting the EMG system. Figs. 1a,2c, 5a and 8c were created with BioRender.com.

Data availability statement

The data that support the findings of this study are available from Zenodo at https://doi.org/10.5281/zenodo.11223073. Matlab scripts for reproducing the findings of this study are available at https://github.com/neuromotion/The_HD64.

Financial support

This work was sponsored in part by the Defense Advanced Research Projects Agency (DARPA) BTO under the auspices of Drs. Alfred Emondi, Jean-Paul Chretien, and Pedro Irazoqui (through the Space and Naval Warfare Systems Center, Pacific DARPA Contracts Management Office) grant/contract numbers D15AP00112 and D19AC00015 to DAB, and by the Merit Review Award #I01RX002835 from the United States Department of Veterans Affairs (VA), Rehabilitation Research and Development Service to DAB. This work was supported in part by the Center for Neurorestoration and Neurotechnology (N2864-C) from the United States (U.S.) Department of Veterans Affairs, Rehabilitation research and Development Service, Providence, RI. The contents of this manuscript do not represent the views of the U.S. Department of Veterans Affairs or the United States Government. Computing resources were provided by the Brown University Center for Computation and Visualization (CCV) using the Carney Condo, supported by National Institute of Health (NIH) Office of the Director grant S10OD025181 (Jerome Sanes). SRP was supported by the 2020 Susan and Isaac Wakil Foundation John Monash Scholarship. JSC was supported by the National Institute for Neurological Disorders and Stroke (NINDS) T32 Postdoctoral Training Program in Recovery and Restoration of Central Nervous System Health and Function (5T32NS100663-04) under the guidance of DAB. JJ was supported by the Basic Science Research Program through the National Research Foundation of Korea (NRF) funded by the Ministry of Education (RS-2023-00246822). LNG was supported by the 2021-2022 Carney Institute for Brain Science Graduate Fellowship under the guidance of TS. BM, YI, KA, and GC were supported in part by the National Institute for Neurological Disorders and Stroke (NINDS) grant U44NS115111.

Authorship statement

All authors contributed to the conception and design of the project. KA and GC designed and manufactured the HD64 paddles. BM and YI developed the HD64 system. JF, ES, and RD performed the spinal implant surgeries. JJ and LNG designed the neural network models. SRP, JSC, and RD acquired and preprocessed data. SRP, JSC, RD, JJ, LNG, TS, and DAB interpreted and analyzed data. All authors assisted with drafting the manuscript and reviewed study results. Final approval was given by all authors.

Conflict of interest

SRP, JSC, RD, and DAB have patents pending regarding the recording of spinal electrophysiological signals during spinal cord stimulation (PCT-US2022-034450: “A novel method to modulate nervous system activation based on one or more spinal field potentials”). BM, KA, GC have patents and pending patents related to high-resolution spinal cord stimulator devices (US-11116964-B2: “Multi-electrode array with unitary body”, 11027122: “Spinal cord stimulation method to treat lateral neural tissues”, US-11395924-B2: “Implantable devices with

787 welded multi-contact electrodes and continuous conductive elements”). Micro-Leads Medical is
788 a commercial company developing precision neuromodulation therapeutic devices and BM, KA,
789 GC, and YI are shareholders or have stock options in Micro-Leads.
790

791 **References**

792 Angeli CA, Boakye M, Morton RA, Vogt J, Benton K, Chen Y, Ferreira CK, Harkema SJ. 2018.
793 Recovery of Over-Ground Walking after Chronic Motor Complete Spinal Cord Injury. *N Engl*
794 *J Med* **379**:1244–1250. doi:10.1056/NEJMoa1803588
795 Badi M, Wurth S, Scarpato I, Roussinova E, Losanno E, Bogaard A, Delacombaz M, Borgognon
796 S, C Vanc Ara P, Fallegger F, Su DK, Schmidlin E, Courtine G, Bloch J, Lacour SP,
797 Stieglitz T, Rouiller EM, Capogrosso M, Micera S. 2021. Intrafascicular peripheral nerve
798 stimulation produces fine functional hand movements in primates. *Sci Transl Med*
799 **13**:eabg6463. doi:10.1126/scitranslmed.abg6463
800 Bonizzato M, Guay Hottin R, Côté SL, Massai E, Choinière L, Macar U, Laferrière S, Sirpal P,
801 Quessy S, Lajoie G, Martinez M, Dancause N. 2023. Autonomous optimization of
802 neuroprosthetic stimulation parameters that drive the motor cortex and spinal cord outputs
803 in rats and monkeys. *Cell Rep Med* **4**:101008. doi:10.1016/j.xcrm.2023.101008
804 Boston Scientific. 2020. Surgical Leads Directions for Use [User manual].
805 Bryson N, Lombardi L, Hawthorn R, Fei J, Keesey R, Peiffer JD, Seáñez I. 2023. Enhanced
806 selectivity of transcutaneous spinal cord stimulation by multielectrode configuration. *J*
807 *Neural Eng* **20**. doi:10.1088/1741-2552/ace552
808 Burke JF, Kunwar N, Yaroshinsky MS, Louie KH, Shirvalkar P, Su P, Henry M, Pasvankas G,
809 Poree L, Jacques L, Wang DD. 2021. Epidural Spinal Electrogram Provides Direct Spinal
810 Recordings in Awake Human Participants. *Front Hum Neurosci* **15**:721076.
811 doi:10.3389/fnhum.2021.721076
812 Calvert JS, Darie R, Parker SR, Shaaya E, Syed S, McLaughlin BL, Fridley JS, Borton DA.
813 2023. Spatiotemporal Distribution of Electrically Evoked Spinal Compound Action
814 Potentials During Spinal Cord Stimulation. *Neuromodulation* **26**:961–974.
815 doi:10.1016/j.neurom.2022.03.007
816 Calvert JS, Manson GA, Grahn PJ, Sayenko DG. 2019. Preferential activation of spinal
817 sensorimotor networks via lateralized transcutaneous spinal stimulation in neurologically
818 intact humans. *J Neurophysiol* **122**:2111–2118. doi:10.1152/jn.00454.2019
819 Capogrosso M, Milekovic T, Borton D, Wagner F, Moraud EM, Mignardot J-B, Buse N, Gandar
820 J, Barraud Q, Xing D, Rey E, Duis S, Jianzhong Y, Ko WKD, Li Q, Detemple P, Denison T,
821 Micera S, Bezard E, Bloch J, Courtine G. 2016. A brain-spine interface alleviating gait
822 deficits after spinal cord injury in primates. *Nature* **539**:284–288. doi:10.1038/nature20118
823 Capogrosso M, Wenger N, Raspopovic S, Musienko P, Beauparlant J, Bassi Luciani L, Courtine
824 G, Micera S. 2013. A computational model for epidural electrical stimulation of spinal
825 sensorimotor circuits. *J Neurosci* **33**:19326–19340. doi:10.1523/JNEUROSCI.1688-
826 13.2013
827 Chakravarthy K, Bink H, Dinsmoor D. 2020. Sensing Evoked Compound Action Potentials from
828 the Spinal Cord: Novel Preclinical and Clinical Considerations for the Pain Management
829 Researcher and Clinician. *J Pain Res* **13**:3269–3279. doi:10.2147/JPR.S289098
830 Chamanzar M, Malekoshoaraie M, Wu B, Krahe D, Ahmed Z, Pupa S, Jain V, Cui XT. 2023.
831 Fully flexible high-density implantable neural probes for electrophysiology recording and
832 controlled neurochemical modulation. *Research Square*. doi:10.21203/rs.3.rs-2720944/v1
833 Chandrasekaran S, Nanivadekar AC, McKernan G, Helm ER, Boninger ML, Collinger JL, Gaunt
834 RA, Fisher LE. 2020. Sensory restoration by epidural stimulation of the lateral spinal cord in
835 upper-limb amputees. *Elife* **9**. doi:10.7554/eLife.54349

Falowski SM. 2019. An Observational Case Series of Spinal Cord Stimulation Waveforms Visualized on Intraoperative Neuromonitoring. *Neuromodulation* **22**:219–228. doi:10.1111/ner.12781

Gad PN, Roy RR, Zhong H, Lu DC, Gerasimenko YP, Edgerton VR. 2014. Initiation of bladder voiding with epidural stimulation in paralyzed, step trained rats. *PLoS One* **9**:e108184. doi:10.1371/journal.pone.0108184

Gill ML, Grahn PJ, Calvert JS, Linde MB, Lavrov IA, Strommen JA, Beck LA, Sayenko DG, Van Straaten MG, Drubach DI, Veith DD, Thoreson AR, Lopez C, Gerasimenko YP, Edgerton VR, Lee KH, Zhao KD. 2018. Neuromodulation of lumbosacral spinal networks enables independent stepping after complete paraplegia. *Nat Med* **24**:1677–1682. doi:10.1038/s41591-018-0175-7

Gorman K. n.d. How to Use UMAP — umap 0.5 documentation. https://umap-learn.readthedocs.io/en/latest/basic_usage.html

Govindarajan LN, Calvert JS, Parker SR, Jung M, Darie R, Miranda P, Shaaya E, Borton DA, Serre T. 2022. Fast inference of spinal neuromodulation for motor control using amortized neural networks. *J Neural Eng* **19**. doi:10.1088/1741-2552/ac9646

Harland TA, Topp G, Shao K, Pilitsis JG. 2022. Revision and Replacement of Spinal Cord Stimulator Paddle Leads. *Neuromodulation* **25**:753–757. doi:10.1016/j.neurom.2022.02.228

Hofstoetter US, Perret I, Bayart A, Lackner P, Binder H, Freundl B, Minassian K. 2021. Spinal motor mapping by epidural stimulation of lumbosacral posterior roots in humans. *iScience* **24**:101930. doi:10.1016/j.isci.2020.101930

Jun JJ, Steinmetz NA, Siegle JH, Denman DJ, Bauza M, Barbarits B, Lee AK, Anastassiou CA, Andrei A, Aydın Ç, Barbic M, Blanche TJ, Bonin V, Couto J, Dutta B, Gratiy SL, Gutnisky DA, Häusser M, Karsh B, Ledochowitsch P, Lopez CM, Mitelut C, Musa S, Okun M, Pachitariu M, Putzeys J, Rich PD, Rossant C, Sun W-L, Svoboda K, Carandini M, Harris KD, Koch C, O'Keefe J, Harris TD. 2017. Fully integrated silicon probes for high-density recording of neural activity. *Nature* **551**:232–236. doi:10.1038/nature24636

Krog L, Maloney J, Pew S, Adeleye O, Johnson B, Glenn B, Gill B, Tieppo Francio V, Pagan-Rosado R, Whitney M, Sinha N, Strand N. 2023. Cervical Spinal Cord Stimulation: A Review. *Curr Pain Headache Rep*. doi:10.1007/s11916-023-01200-8

Letechipia JE, Peckham PH, Gazdik M, Smith B. 1991. In-line lead connector for use with implanted neuroprosthesis. *IEEE Trans Biomed Eng* **38**:707–709. doi:10.1109/10.83572

Logé D, Vanneste S, Vancamp T, Rijckaert D. 2013. Long-term outcomes of spinal cord stimulation with percutaneously introduced paddle leads in the treatment of failed back surgery syndrome and lumboischialgia. *Neuromodulation* **16**:537–45; discussion 545. doi:10.1111/ner.12012

Lorach H, Galvez A, Spagnolo V, Martel F, Karakas S, Intering N, Vat M, Faivre O, Harte C, Komi S, Ravier J, Collin T, Coquoz L, Sakr I, Baaklini E, Hernandez-Charpak SD, Dumont G, Buschman R, Buse N, Denison T, van Nes I, Asboth L, Watrin A, Struber L, Sauter-Starace F, Langar L, Auboiroux V, Carda S, Chabardes S, Aksenova T, Demesmaeker R, Charvet G, Bloch J, Courtine G. 2023. Walking naturally after spinal cord injury using a brain-spine interface. *Nature* **618**:126–133. doi:10.1038/s41586-023-06094-5

Maciejasz P, Badia J, Boretius T, Harreby KR, Jensen W, Stieglitz T, Navarro X, Guiraud D. 2013. Comparison of Stimulation Selectivity in Monopolar and Bipolar Configuration Using the Transversal Intrafascicular Multichannel Electrode (TIME) - Preliminary ResultsConverging Clinical and Engineering Research on Neurorehabilitation. Springer Berlin Heidelberg. pp. 79–83. doi:10.1007/978-3-642-34546-3_13

Marcus MA, Bruyninckx FL, Vertommen JD, Wouters PF, Van Aken H. 1997. Spinal somatosensory evoked potentials after epidural isoproterenol in awake sheep. *Can J Anaesth* **44**:85–89. doi:10.1007/BF03014330

McInnes L, Healy J, Melville J. 2018a. UMAP: Uniform Manifold Approximation and Projection

for Dimension Reduction. *arXiv [statML]*.
McInnes L, Healy J, Saul N, Großberger L. 2018b. UMAP: Uniform Manifold Approximation and Projection. *J Open Source Softw* **3**:861. doi:10.21105/joss.00861
Medtronic. 2022. Product Performance Report: Summary of Data from the Medtronic Post-Market Registry (No. UC202000365eEN). Medtronic.
Mekhail N, Levy RM, Deer TR, Kapural L, Li S, Amirdelfan K, Hunter CW, Rosen SM, Costandi SJ, Falowski SM, Burgher AH, Pope JE, Gilmore CA, Qureshi FA, Staats PS, Scowcroft J, Carlson J, Kim CK, Yang MI, Stauss T, Poree L, Evoke Study Group. 2020. Long-term safety and efficacy of closed-loop spinal cord stimulation to treat chronic back and leg pain (Evoke): a double-blind, randomised, controlled trial. *Lancet Neurol* **19**:123–134. doi:10.1016/S1474-4422(19)30414-4
Mishra LN, Kulkarni G, Gadgil M. 2023. A novel current steering method for targeted spinal cord stimulation. *Front Pain Res (Lausanne)* **4**:1028368. doi:10.3389/fpain.2023.1028368
Musienko P, Courtine G, Tibbs JE, Kilimnik V, Savochin A, Garfinkel A, Roy RR, Edgerton VR, Gerasimenko Y. 2012. Somatosensory control of balance during locomotion in decerebrated cat. *J Neurophysiol* **107**:2072–2082. doi:10.1152/jn.00730.2011
Nahm FS. 2020. From the torpedo fish to the spinal cord stimulator. *Korean J Pain* **33**:97–98. doi:10.3344/kjp.2020.33.2.97
Nainzadeh NK, Neuwirth MG, Bernstein R, Cohen LS. 1988. Direct Recording of Spinal Evoked Potentials to Peripheral Nerve Stimulation by a Specially Modified ElectrodeNeurophysiology and Standards of Spinal Cord Monitoring. Springer New York. pp. 234–244. doi:10.1007/978-1-4612-3804-1_29
Nanivadekar AC, Bose R, Petersen BA, Okorokova EV, Sarma D, Madonna TJ, Barra B, Farooqui J, Dalrymple AN, Levy I, Helm ER, Miele VJ, Boninger ML, Capogrosso M, Bensmaia SJ, Weber DJ, Fisher LE. 2023. Restoration of sensory feedback from the foot and reduction of phantom limb pain via closed-loop spinal cord stimulation. *Nat Biomed Eng*. doi:10.1038/s41551-023-01153-8
Nijhuis HJA, Hofsté W-J, Krabbenbos IP, Dietz BE, Mugan D, Huygen F. 2023. First Report on Real-World Outcomes with Evoked Compound Action Potential (ECAP)-Controlled Closed-Loop Spinal Cord Stimulation for Treatment of Chronic Pain. *Pain Ther* **12**:1221–1233. doi:10.1007/s40122-023-00540-y
Palopoli-Trojani K, Trumpis M, Chiang C-H, Wang C, Williams AJ, Evans CL, Turner DA, Viventi J, Hoffmann U. 2024. High-density cortical µECoG arrays concurrently track spreading depolarizations and long-term evolution of stroke in awake rats. *Commun Biol* **7**:263. doi:10.1038/s42003-024-05932-0
Parker JL, Karantonis DM, Single PS, Obradovic M, Laird J, Gorman RB, Ladd LA, Cousins MJ. 2013. Electrically evoked compound action potentials recorded from the sheep spinal cord. *Neuromodulation* **16**:295–303; discussion 303. doi:10.1111/ner.12053
Parker JL, Laird-Wah J, Cousins MJ. 2018. Comparison of a simple model of dorsal column axons with the electrically evoked compound action potential. *Bioelectronics in Medicine* **1**:117–130. doi:10.2217/bem-2017-0006
Parker JL, Obradovic M, Hesam Shariati N, Gorman RB, Karantonis DM, Single PS, Laird-Wah J, Bickerstaff M, Cousins MJ. 2020. Evoked Compound Action Potentials Reveal Spinal Cord Dorsal Column Neuroanatomy. *Neuromodulation* **23**:82–95. doi:10.1111/ner.12968
Pedregosa F, Varoquaux G, Gramfort A, Michel V, Thirion B, Grisel O, Blondel M, Louppe G, Prettenhofer P, Weiss R, Weiss RJ, Vanderplas J, Passos A, Cournapeau D, Brucher M, Perrot M, Duchesnay E. 2011. Scikit-learn: Machine Learning in Python. *J Mach Learn Res* **abs/1201.0490**. doi:10.5555/1953048.2078195
Rachinskiy I, Wong L, Chiang C-H, Wang C, Trumpis M, Ogren JI, Hu Z, McLaughlin B, Viventi J. 2022. High-Density, Actively Multiplexed µECoG Array on Reinforced Silicone Substrate. *Front Nanotechnol* **4**. doi:10.3389/fnano.2022.837328

Reddy CG, Miller JW, Abode-Iyamah KO, Safayi S, Wilson S, Dalm BD, Fredericks DC, Gillies GT, Howard MA 3rd, Brennan TJ. 2018. Ovine model of neuropathic pain for assessing mechanisms of spinal cord stimulation therapy via dorsal horn recordings, von Frey filaments, and gait analysis. *J Pain Res* **11**:1147–1162. doi:10.2147/JPR.S139843

Rousseeuw PJ. 1987. Silhouettes: A graphical aid to the interpretation and validation of cluster analysis. *J Comput Appl Math* **20**:53–65. doi:10.1016/0377-0427(87)90125-7

Rowald A, Komi S, Demesmaeker R, Baaklini E, Hernandez-Charpak SD, Paoles E, Montanaro H, Cassara A, Becce F, Lloyd B, Newton T, Ravier J, Kinany N, D'Ercole M, Paley A, Hankov N, Varescon C, McCracken L, Vat M, Caban M, Watrin A, Jacquet C, Bole-Feysot L, Harte C, Lorach H, Galvez A, Tschopp M, Herrmann N, Wacker M, Geernaert L, Fodor I, Radevich V, Van Den Keybus K, Eberle G, Pralong E, Roulet M, Ledoux J-B, Fornari E, Mandija S, Mattera L, Martuzzi R, Nazarian B, Benkler S, Callegari S, Greiner N, Fuhrer B, Froeling M, Buse N, Denison T, Buschman R, Wende C, Ganty D, Bakker J, Delattre V, Lambert H, Minassian K, van den Berg CAT, Kavounoudias A, Micera S, Van De Ville D, Barraud Q, Kurt E, Kuster N, Neufeld E, Capogrosso M, Asboth L, Wagner FB, Bloch J, Courtine G. 2022. Activity-dependent spinal cord neuromodulation rapidly restores trunk and leg motor functions after complete paralysis. *Nat Med* **28**:260–271. doi:10.1038/s41591-021-01663-5

Shi J, Malik J. 2000. Normalized cuts and image segmentation. *IEEE Trans Pattern Anal Mach Intell* **22**:888–905. doi:10.1109/34.868688

Shils JL, Arle JE. 2018. Neuromonitoring for Spinal Cord Stimulation Lead Placement Under General Anesthesia. *J Clin Neurol* **14**:444–453. doi:10.3988/jcn.2018.14.4.444

Solinsky R, Specker-Sullivan L, Wexler A. 2020. Current barriers and ethical considerations for clinical implementation of epidural stimulation for functional improvement after spinal cord injury. *J Spinal Cord Med* **43**:653–656. doi:10.1080/10790268.2019.1666240

Steinmetz NA, Aydin C, Lebedeva A, Okun M, Pachitariu M, Bauza M, Beau M, Bhagat J, Böhm C, Broux M, Chen S, Colonell J, Gardner RJ, Karsh B, Kloosterman F, Kostadinov D, Mora-Lopez C, O'Callaghan J, Park J, Putzeys J, Sauerbrei B, van Daal RJJ, Vollan AZ, Wang S, Welkenhuysen M, Ye Z, Dudman JT, Dutta B, Hantman AW, Harris KD, Lee AK, Moser EI, O'Keefe J, Renart A, Svoboda K, Häusser M, Haesler S, Carandini M, Harris TD. 2021. Neuropixels 2.0: A miniaturized high-density probe for stable, long-term brain recordings. *Science* **372**. doi:10.1126/science.abf4588

Wilson S, Abode-Iyamah KO, Miller JW, Reddy CG, Safayi S, Fredericks DC, Jeffery ND, DeVries-Watson NA, Shivapour SK, Viljoen S, Dalm BD, Gibson-Corley KN, Johnson MD, Gillies GT, Howard MA 3rd. 2017. An ovine model of spinal cord injury. *J Spinal Cord Med* **40**:346–360. doi:10.1080/10790268.2016.1222475

Woodington BJ, Lei J, Carnicer-Lombarte A, Güemes-González A, Naegele TE, Hilton S, El-Hadwe S, Trivedi RA, Malliaras GG, Barone DG. 2024. Flexible circumferential bioelectronics to enable 360-degree recording and stimulation of the spinal cord. *Sci Adv* **10**:eadl1230. doi:10.1126/sciadv.adl1230

Yeo I, Johnson RA. 2000. A new family of power transformations to improve normality or symmetry. *Biometrika* **87**:954–959. doi:10.1093/biomet/87.4.954

Zhao Z, Ahmadi A, Hoover C, Grado L, Peterson N, Wang X, Freeman D, Murray T, Lamperski A, Darrow D, Netoff TI. 2021. Optimization of Spinal Cord Stimulation Using Bayesian Preference Learning and Its Validation. *IEEE Trans Neural Syst Rehabil Eng* **29**:1987–1997. doi:10.1109/TNSRE.2021.3113636

Zhu Z, Tang Q, Zeng F-G, Guan T, Ye D. 2012. Cochlear-implant spatial selectivity with monopolar, bipolar and tripolar stimulation. *Hear Res* **283**:45–58. doi:10.1016/j.heares.2011.11.005

Figures & Captions

Figure 1

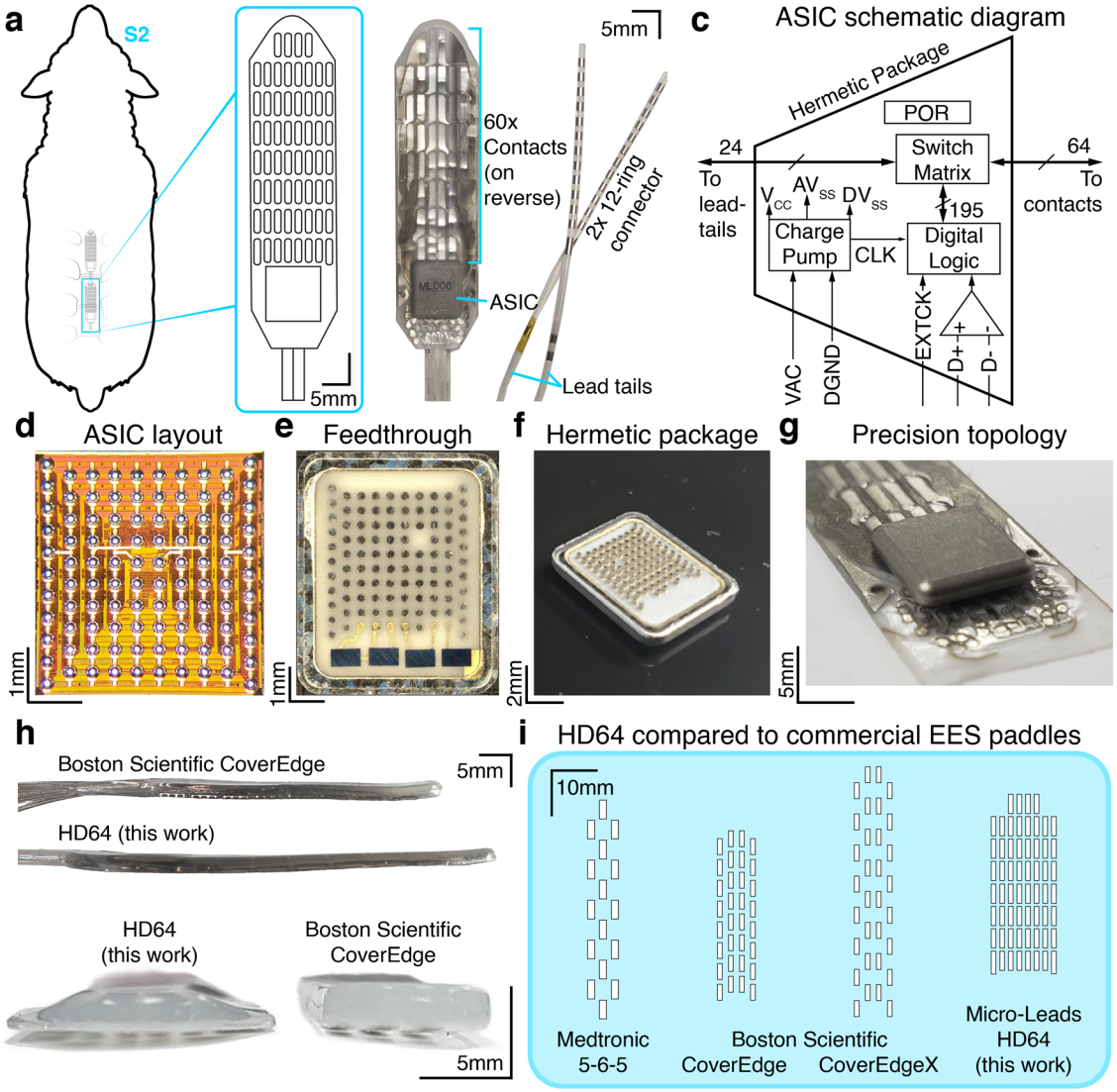

(a) A scale diagram of the layout of the HD64. (b) A photograph of the HD64. (c) A block diagram of the integrated circuitry of the ASIC. The element labeled “POR” handles the power-on-reset functionality of the ASIC. (d) A photograph of the ASIC following tape-out. (e) The ASIC flip-chipped to the hermetic feedthrough array of pins. (f) The electronics package feedthrough array, hermetically sealed with a laser seam-weld. The interior of the package contains a hermetic feedthrough array. (g) The electronics package affixed to the electrode substrate, prior to encapsulation. (h) Comparing the physical dimensions of the electrode paddle developed in this work (the HD64) with other commercial paddles.

Figure 2

In vivo evaluation of the HD64 in an ovine model

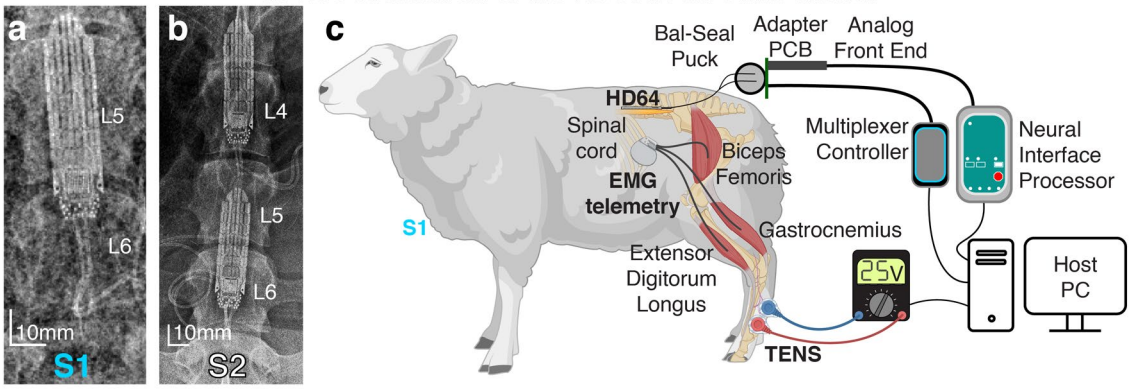

(a, b) Radiographs showing the HD64 implanted in the sheep S1 and S2 respectively, with vertebral levels labeled. (c) A schematic overview of the experimental setup. The host PC controls the collection of spinal electrophysiology, application of transcutaneous electrical nerve stimulation (TENS) and epidural electrical stimulation (EES), and the configuration of the onboard ASIC through the multiplexer controller. In S1 and S2, electromyographic (EMG) signals are collected from implanted, wireless intramuscular EMG telemetry devices or wireless surface EMG devices, respectively.

Figure 3

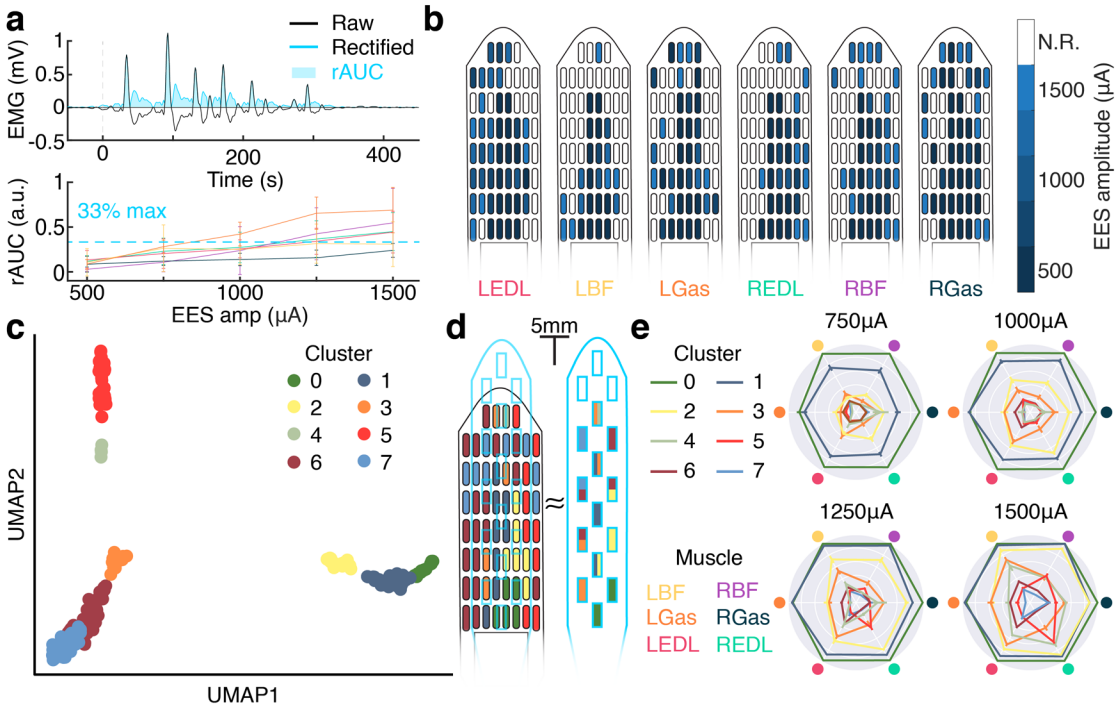

Clustering analysis of motor outputs evoked by monopolar stimulation. (a) A graphical overview of the electromyography (EMG) preprocessing. A representative EMG trace (black) is rectified (blue trace), then the rectified area under the curve is calculated (blue shaded region). A sample recruitment curve is shown for six muscles. The points are the mean, and the bars show the standard deviation. A blue dashed line indicates the 33% of maximum activation threshold used for panel (b). (b) The minimum required epidural electrical stimulation (EES) amplitude required to recruit each of the six instrumented muscles to 33% of their maximum activation. Electrodes marked “N.R.” could not recruit the muscle to 33% of its maximum activation at the amplitude range tested. (c) A 2D projection of the embedded recruitment data. Each point is a stimulation event, and the points are colored by which cluster the stimulating electrode resides in. (d) A diagram of the HD64, with the electrode contacts colored by which cluster the electrode resides in. A scale drawing of the Medtronic 5-6-5 is overlaid to highlight which cluster(s) each of the 5-6-5’s electrodes contact. (e) Representative radar plots (EES frequency = 50Hz) show the mean responses for each stimulation contact cluster. The clusters exhibit diverse recruitment patterns and relationships with amplitude.

Figure 4

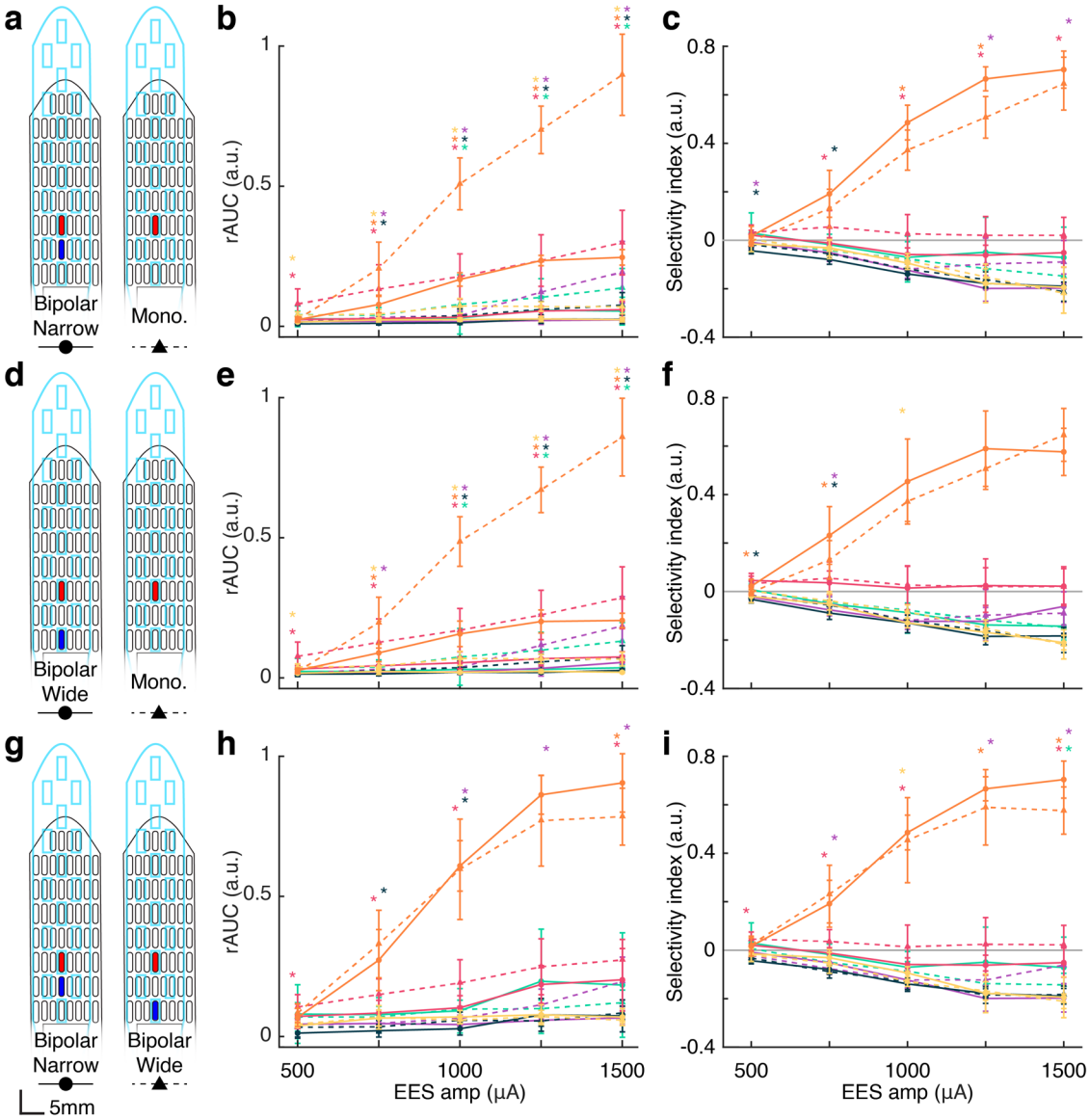

(a, d, g) The stimulation cathode (red) and anode (blue) for the bipolar configurations, and the cathode for the monopolar configurations. In the monopolar configurations, the stimulation current return contact was a wire implanted in the paraspinal muscles. (b, e, h) Recruitment curves for each stimulation contact configuration presented in the left-hand column. Points are the mean recruitment, and the bars are the standard deviation. (c, f, i) Selectivity index as a function of amplitude for each stimulation contact configuration presented in the left-hand column. Points are the mean recruitment, and the bars are the standard deviation. Statistical significance was calculated using a Kruskal-Wallis non-parametric test, with a maximum *p*-value of 0.05.

Figure 5

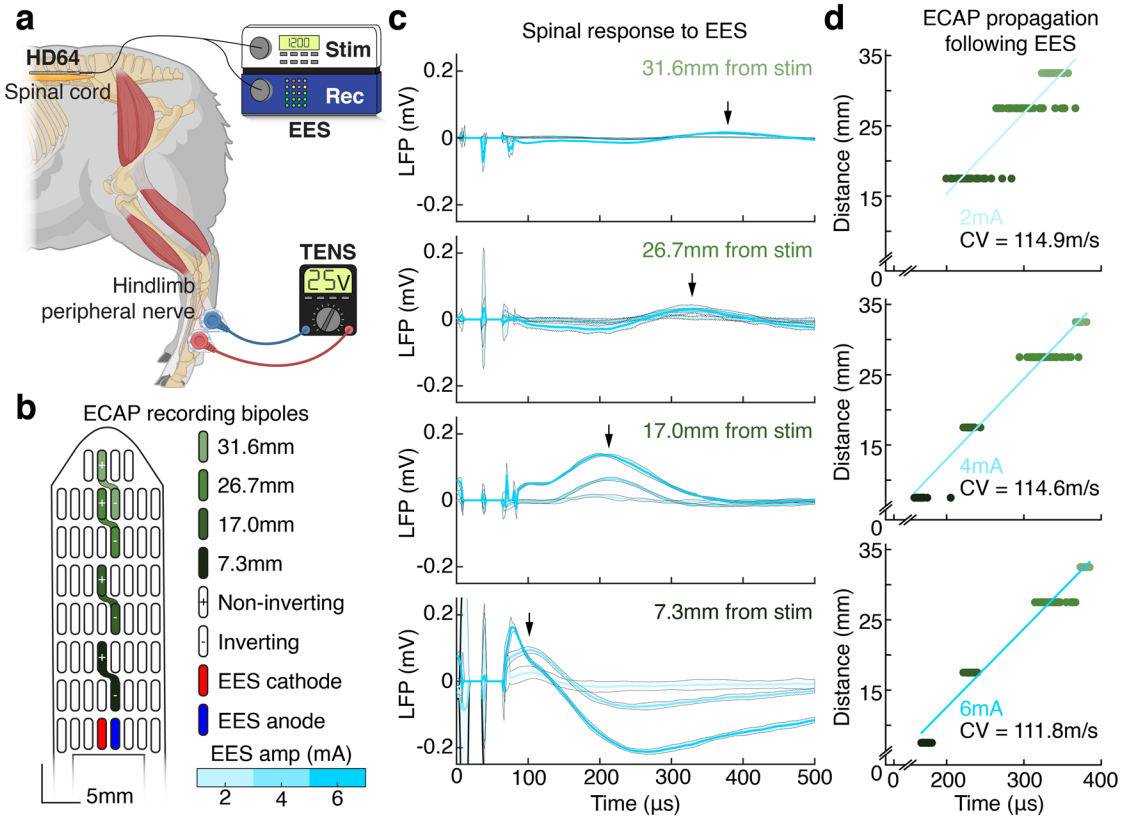

Assessing spinal responses detected by monopolar, wide bipolar, and narrow bipolar recordings. (a) A graphical overview of the spinal local field potential (LFP) recording, epidural electrical stimulation (EES) and transcutaneous electrical nerve stimulation (TENS) setup. (b) A map of the HD64, showing the stimulation cathode (red) and anode (blue). The recording bipoles and their distances from stimulation are shown. (c) The mean and standard deviation of the spinal evoked compound action potential (ECAP) response recorded using various bipolar pairs along the midline of the spinal cord, for three stimulation amplitudes. The peak of the 4mA stimulation response is shown with a black arrow. Note that peak latency increases with separation from the stimulation bipole. (d) The peak latencies of 50 single trials, plotted as a function of separation from the stimulating bipole, for each stimulation amplitude. The samples are colored by their recording bipole. A linear fit is plotted in blue, with the conduction velocity (CV) inset.

1068 **Figure 6**

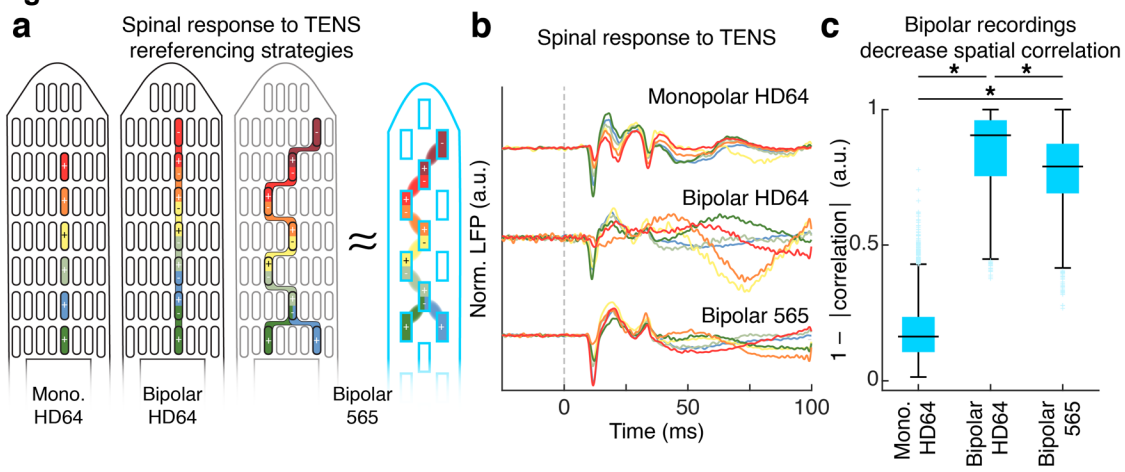

1069

1070 (a) A map of the recording contacts for the three recording configurations. In monopolar
1071 configurations, the recording reference was a wire implanted in the epidural space. (b) The
1072 mean sensorimotor evoked potentials (SEPs) recorded from 50 TENS stimulation events (TENS
1073 amplitude = 25V) for each of the three recording configurations. (c) The distribution of spatial
1074 uniqueness scores (1 - |correlation|) achieved for each of the three recording configurations.
1075 The black horizontal bar is the median, and the boxes extend from the 25th to the 75th
1076 percentile. Statistical significance was calculated using a Kruskal-Wallis non-parametric test,
1077 with a maximum *p*-value of 0.05.

1078

Figure 7

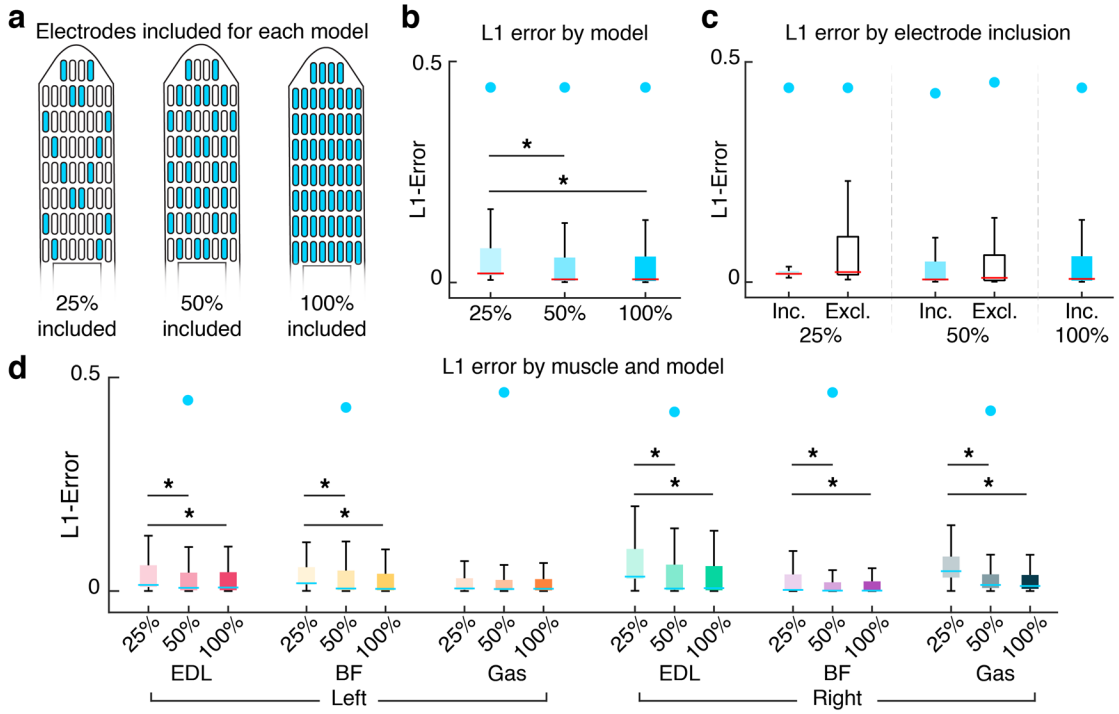

Evaluating the performance of the forward neural network model to predict sensorimotor computations. In all boxplots the horizontal bar is the median, the boxes extend from the 25th to the 75th percentile, and the blue dots represent a “random” baseline performance. (a) A map of the electrode contacts included in the training dataset for each model. Included electrodes are shaded blue. (b) The distribution of L1 errors between the ground truth and simulated electromyography (EMG) for a held out dataset of 480 stimulation parameter combinations for the three models. (c) The data in (a) split by inclusion of the stimulating electrode in the training dataset. (d) The data in (a) split by muscle. Statistical significance was calculated using a Kruskal-Wallis non-parametric test, with a maximum *p*-value of 0.05.

Figure 8

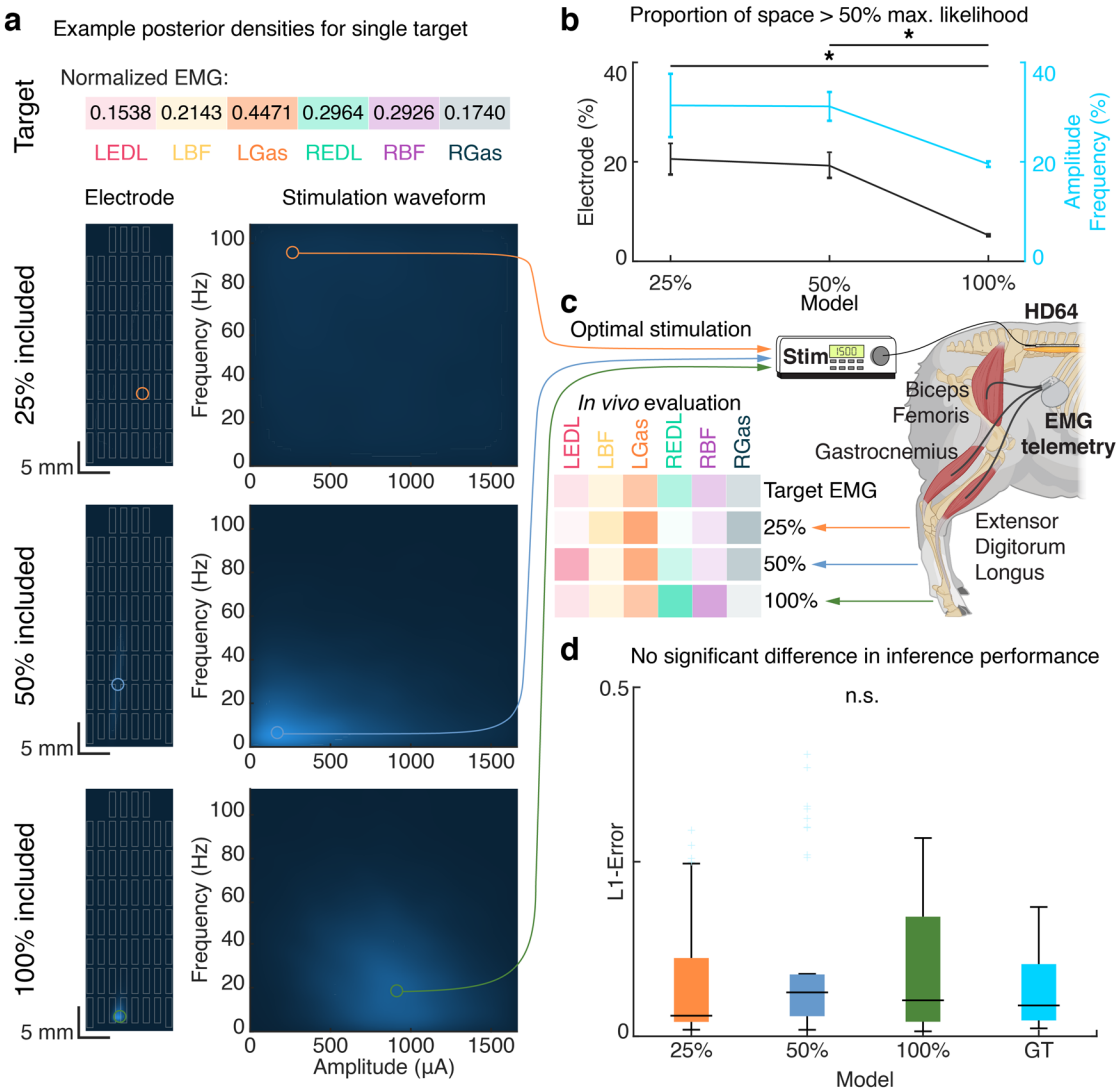

(a) An example target normalized electromyography (EMG) vector is shown at the top. The posterior densities over are shown for 3 models. Higher likelihood regions are indicated in lighter colors. (b) A plot showing the proportion of electrode- and stimulation parameter-space with a likelihood greater than 50% of the maximum likelihood for that prediction. The samples are the mean, and the bars are the variance. (c) The *in vivo* evaluation procedure. The posterior densities of each model are sampled to produce proposed stimulation parameter combinations for each target. These parameters are applied *in vivo*, and the evoked EMG vector is calculated. The L1-error between the target EMG vector and the evoked EMG vector is then computed. (d) The distribution of mean L1 errors between the target EMG vector and the evoked EMG vector for each of the three models, and between EMG vectors evoked using identical stimuli in the training and evaluation sessions (“ground truth”, or GT).

1105 **Table 1**
1106 A comparison of the physical characteristics of commercially available epidural electrical
1107 stimulation paddles and the paddle developed in this work, the HD64.

	5-6-5 (Medtronic, 2022)	**CoverEdge/X** (Boston Scientific, 2020)	**HD64 (this work)**
Manufacturer	Medtronic (Minneapolis, MN)	Boston Scientific (Marlborough, MA)	Micro-Leads Medical (Somerville, MA)
Length	64.2mm	50mm / 67mm	57.5mm
Width	10mm	9mm / 10mm	14.5 mm
Thickness	2.0 mm	2.0 mm	0.2 mm edge, 2.0 middle
Number of contacts	16	32	60
Inter-electrode spacing (mediolateral, rostrocaudal)	(1.0mm, 4.5mm)	(1.0mm, 1.0mm) / (1.0mm, 3.2mm)	(0.7mm, 0.9mm)
Density vs 5-6-5	1	2.1 / 1.4	2.2
Number of percutaneous lead-tails	2	4	2
Percutaneous lead-tail surface area (50 cm)	41 cm^2	82 cm^2	41 cm^2
Contact surface area	6mm^2	3.4mm^2	4.15mm^2
Contains an active multiplexer	No	No	Yes

1108
1109

Supplementary Figures

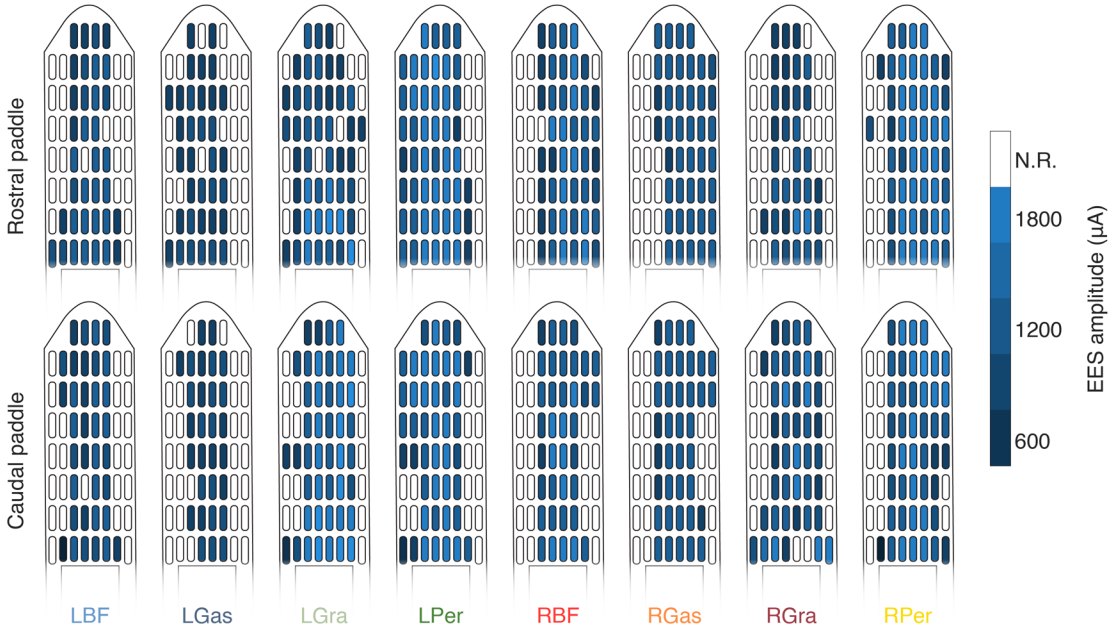

Figure 3 – figure supplement 1

Epidural electrical stimulation amplitude thresholds for S2. Electrode contacts on the rostral and caudal paddles are colored by the minimum required epidural electrical stimulation (EES) amplitude required to recruit each of the six instrumented muscles to 33% of their maximum activation. Electrodes marked “N.R.” could not recruit the muscle to 33% of its maximum activation at the amplitude range tested.

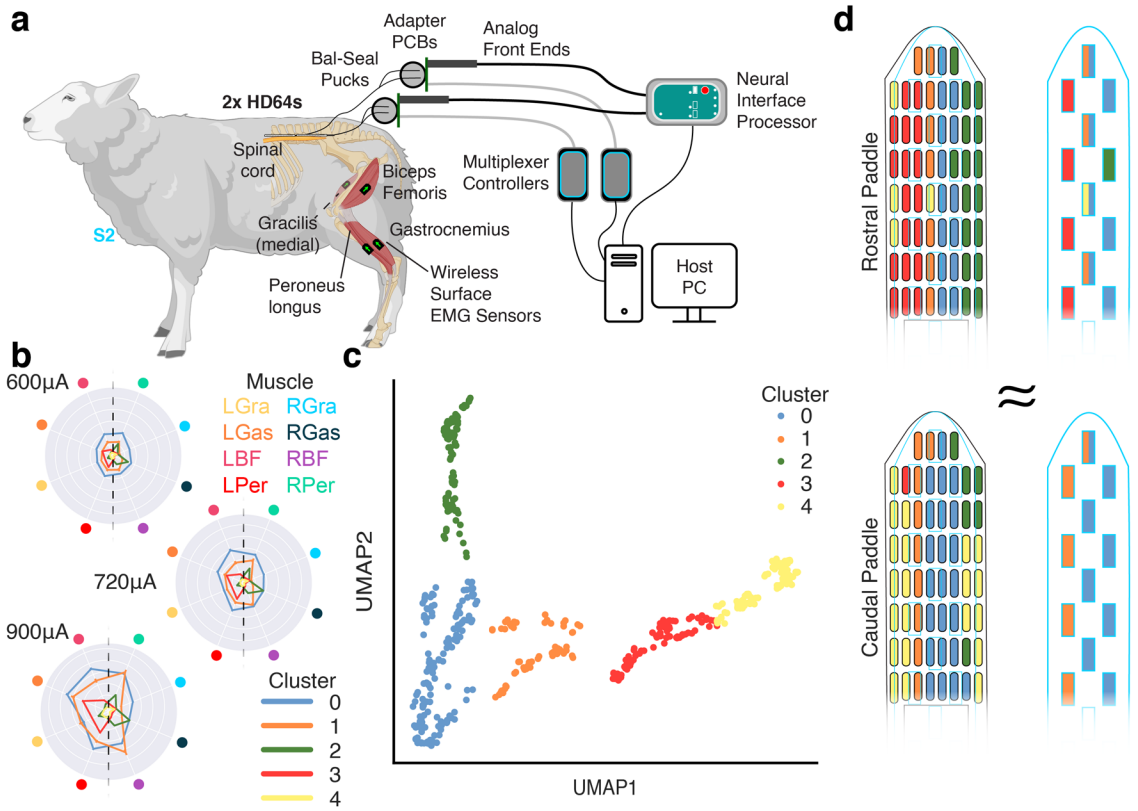

Figure 3 – figure supplement 2

Algorithmic clustering of stimulation-evoked motor responses in S2. (a) A diagram of the experimental setup. In contrast to S1, S2 uses surface electromyography (EMG) sensors, instruments four bilateral hindlimb muscles, and stimulation is applied on two HD64 paddles. (b) Representative radar plots (EES frequency = 50Hz) show the mean responses for each stimulation contact cluster. The clusters exhibit diverse recruitment patterns and relationships with amplitude. (c) A 2D projection of the embedded recruitment data. Each point is a stimulation event, and the points are colored by which cluster the stimulating electrode resides in. (d) A diagram of the two HD64s, with the electrode contacts colored by which cluster the electrode resides in. A scale drawing of the Medtronic 5-6-5 is overlaid to highlight which cluster(s) each of the 5-6-5's electrodes contact.

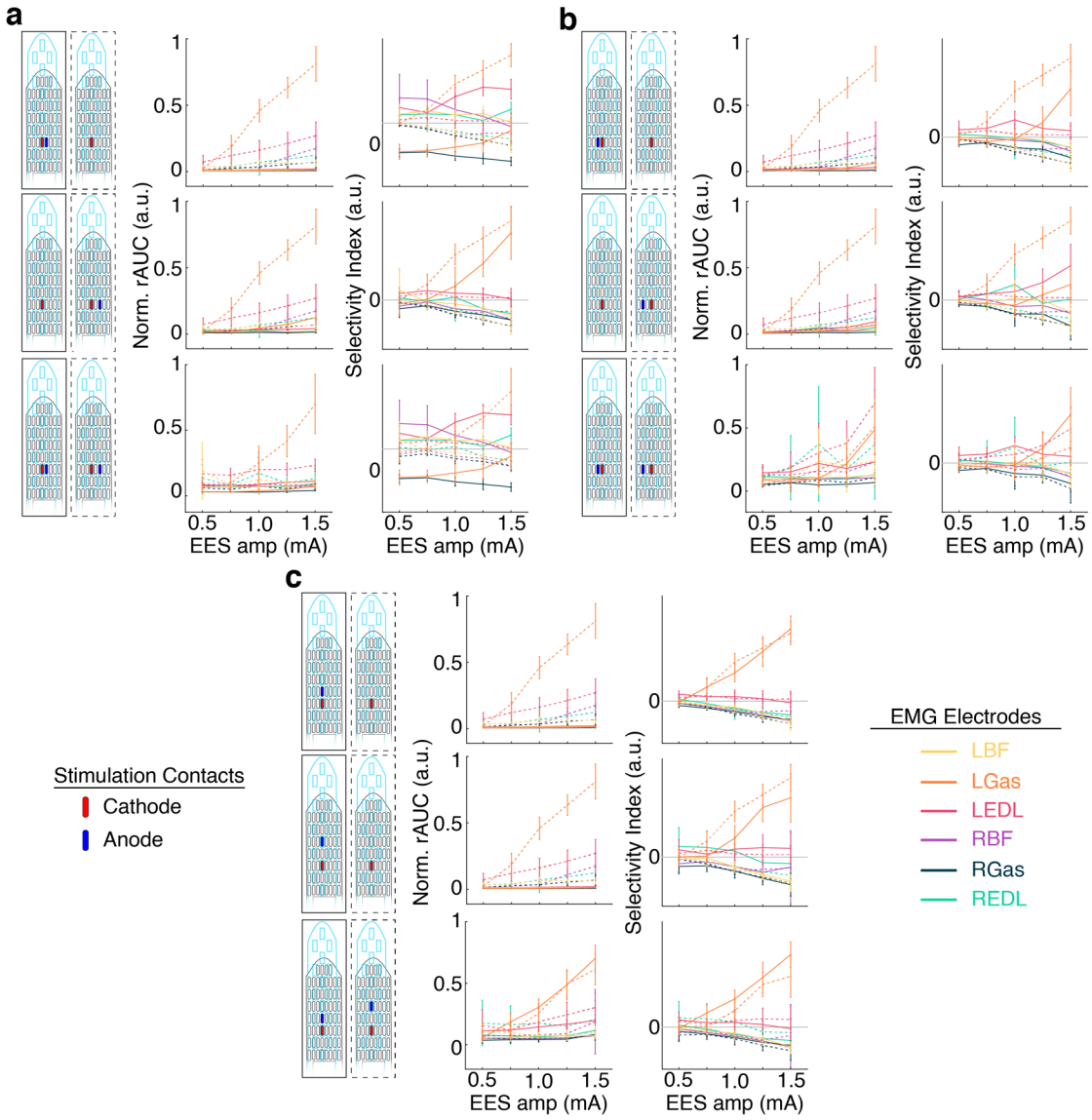

Figure 4 – figure supplement 1

Additional current-steering stimulation-evoked motor response examples. (a-c) Left column: the stimulation configuration. Red contacts are cathode-leading, blue contacts are anode-leading. An outline of the Medtronic 5-6-5 is shown in blue. The responses to the stimulation shown in the solid border are shown with a solid line in the following columns. In monopolar configurations, the stimulation return was a ground wire implanted in the paraspinal muscles. Middle column: the normalized rectified area under the curve of the electromyography (EMG) responses. Right column: the selectivity indexes of the evoked responses.

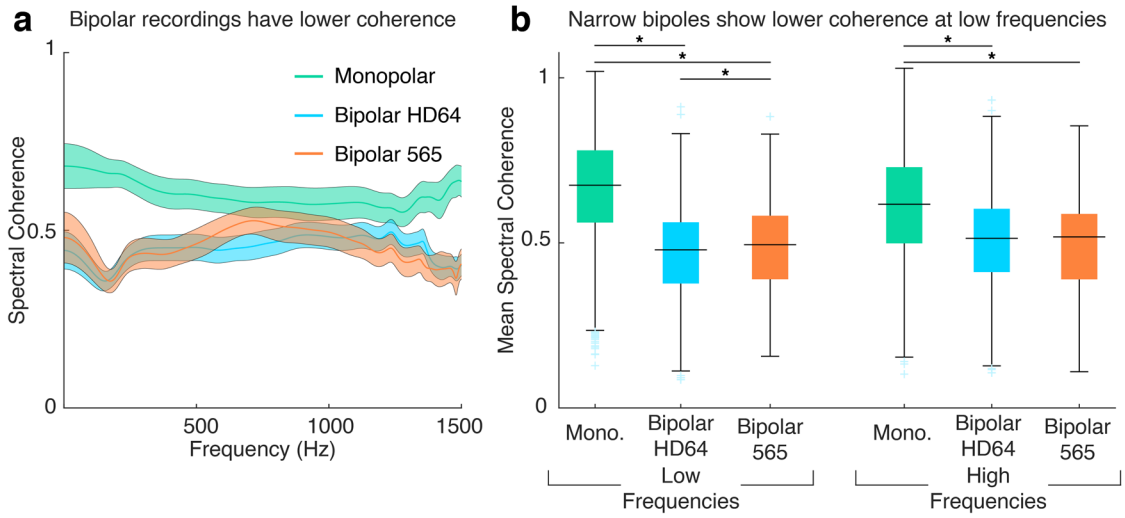

Figure 6 – figure supplement 1

Spectral comparison of spinal local field potentials. (a) The mean and variance of the pairwise magnitude squared coherence for each channel. High coherence values indicate that all channels record that frequency with equal power. (b) A boxplot showing mean magnitude squared coherence values. Results are shown for low frequencies (f < 800Hz) and high frequencies (f ≥ 800Hz). Statistical significance was calculated using a Kruskal-Wallis non-parametric test, with a maximum *p*-value of 0.05.

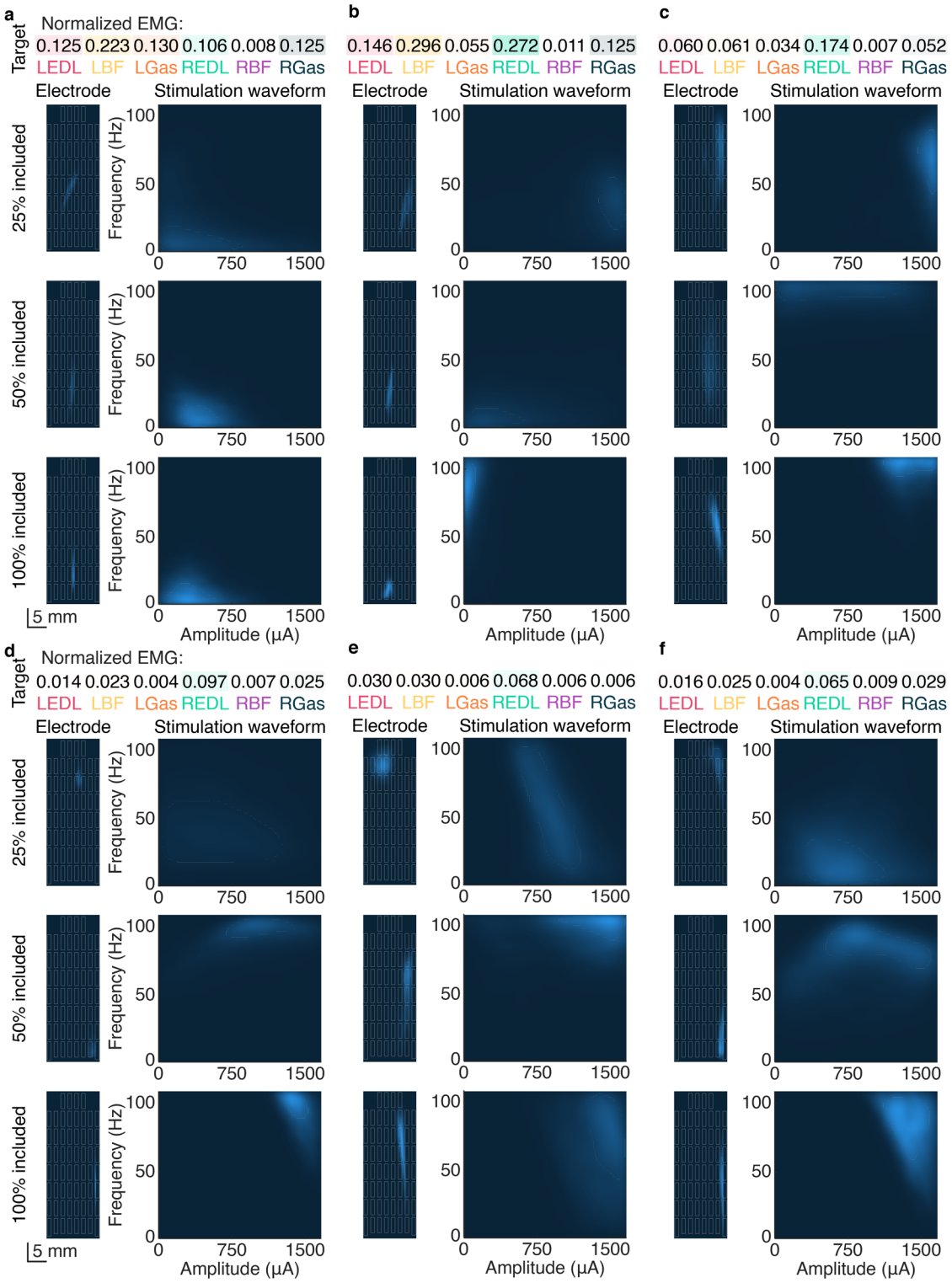

Figure 8 – figure supplement 1

Additional EMG parameter inference posteriors predicted by the inverse model. (a-f) Posterior likelihood densities for electrode- and amplitude-frequency-space predicted by the 25%, 50% and 100% electrode coverage models. High likelihood regions are shown in lighter colors.